



DENSITY FUNCTIONAL THEORY INVESTIGATION OF  $\text{TiO}_2$  ANATASE  
NANOSHEETS

A THESIS SUBMITTED TO  
THE GRADUATE SCHOOL OF NATURAL AND APPLIED SCIENCES  
OF  
MIDDLE EAST TECHNICAL UNIVERSITY

BY

CEREN SİBEL SAYIN

IN PARTIAL FULFILLMENT OF THE REQUIREMENTS  
FOR  
THE DEGREE OF MASTER OF SCIENCE  
IN  
PHYSICS

SEPTEMBER 2009

Approval of the thesis:

**DENSITY FUNCTIONAL THEORY INVESTIGATION OF TiO<sub>2</sub> ANATASE  
NANOSHEETS**

submitted by **CEREN SİBEL SAYIN** in partial fulfillment of the requirements for  
the degree of **Master of Science in Physics Department, Middle East Technical  
University** by,

Prof. Dr. Canan Özgen  
Dean, Graduate School of **Natural and Applied Sciences**

\_\_\_\_\_

Prof. Dr. Sinan Bilikmen  
Head of Department, **Physics**

\_\_\_\_\_

Assist. Prof. Dr. Hande Toffoli  
Supervisor, **Physics Department, METU**

\_\_\_\_\_

Prof. Dr. Şinasi Ellialtıođlu  
Co-supervisor, **Physics Department, METU**

\_\_\_\_\_

**Examining Committee Members:**

Prof. Dr. Mehmet Çakmak  
Physics Department, Gazi University

\_\_\_\_\_

Assist. Prof. Dr. Hande Toffoli  
Physics Department, METU

\_\_\_\_\_

Prof. Dr. Şinasi Ellialtıođlu  
Physics Department, METU

\_\_\_\_\_

Assoc. Prof. Dr. Ersen Mete  
Physics Department, Balıkesir University

\_\_\_\_\_

Prof. Dr. Raşit Turan  
Physics Department, METU

\_\_\_\_\_

**Date:** 11.09.2009

**I hereby declare that all information in this document has been obtained and presented in accordance with academic rules and ethical conduct. I also declare that, as required by these rules and conduct, I have fully cited and referenced all material and results that are not original to this work.**

Name, Last Name: CEREN SİBEL SAYIN

Signature :

## ABSTRACT

### DENSITY FUNCTIONAL THEORY INVESTIGATION OF TiO<sub>2</sub> ANATASE NANOSHEETS

Sayın, Ceren Sibel

M.S., Department of Physics

Supervisor : Assist. Prof. Dr. Hande Toffoli

Co-Supervisor : Prof. Dr. Şinasi Ellialtıođlu

September 2009, 48 pages

In this thesis, the electronic properties of nanosheets derived from TiO<sub>2</sub> anatase structure which acts as a photocatalyst, are investigated using the density functional theory. We examine bulk constrained properties of the nanosheets derived from the (001) surface and obtain their optimized geometries. We investigate properties of lepidocrocite-type TiO<sub>2</sub> nanosheets and nanotubes of different sizes formed by rolling the lepidocrocite nanosheets. We show that the stability and the band gaps of the considered nanotubes increase with increasing diameter. We also study adsorption of Au<sub>n</sub> clusters with (n=1,2,3,4) on the clean and oxygen depleted lepidocrocite surface. Through systematic investigation of various cases we conclude that Au prefers O vacancy sites rather than clean surface in accordance with previous metal adsorption studies on TiO<sub>2</sub> surfaces. For the clean surface, we observe that Au clusters with an odd number of atoms are weakly bonded and metallizes the system while even number of Au atoms results in small band gap semiconductors with relatively higher binding energies.

Keywords: TiO<sub>2</sub> Nanosheets, TiO<sub>2</sub> Nanotubes, Au Adsorption, Density Functional Theory

## ÖZ

### TiO<sub>2</sub> ANATAZ NANO TABAKALARININ YOĞUNLUK FONKSİYONELİ TEORİSİ İLE İNCELENMESİ

Sayın, Ceren Sibel

Yüksek Lisans, Fizik Bölümü

Tez Yöneticisi : Y. Doç. Dr. Hande Toffoli

Ortak Tez Yöneticisi : Prof. Dr. Şinasi Ellialtıođlu

Eylül 2009, 48 sayfa

Bu tezde, photokatalist olarak işlev gören TiO<sub>2</sub> anataz yapısından elde edilmiş nanotabakaların elektronik özellikleri yoğunluk fonksiyoneli teorisi kullanılarak araştırıldı. (001) yüzeyinden elde edilmiş nanotabakaların kütleyle sınırlandırılmış özellikleri çalışıldı ve optimize geometrileri elde edildi. Lepidokrosit tipindeki TiO<sub>2</sub> nanotabakaların ve bunların bükülmesiyle oluşturulmuş farklı boyutlardaki nanotüplerin nitelikleri ortaya konuldu. İncelenen nanotüplerin kararlılıklarının ve bant aralıklarının artan çapla beraber arttığı gösterildi. Ayrıca, (n=1,2,3,4) olmak üzere Au<sub>n</sub> kümelerinin temiz ve oksijeni azaltılmış lepidokrosit yüzeyine adsorpsiyonu çalışıldı. Çeşitli durumların sistematik araştırılmasıyla, önceki çalışmalarla uyumlu olarak Au atomunun O boşluklarını tercih ettiği belirlendi. Temiz yüzeylerde de, tek sayıda atoma sahip Au kümelerinin zayıf bağlar oluşturup sistemi metalle ettiđi, çift sayıda atoma sahip Au kümelerininse daha güçlü bağlanıp dar bant aralıklı yarı iletken sistemlere yol açtığı gözlemlendi.

Anahtar Kelimeler: TiO<sub>2</sub> Nanotabakaları, TiO<sub>2</sub> Nanotüpleri, Au Adsorpsiyonu, Yoğunluk Fonksiyoneli Teorisi

*To my mother*

## ACKNOWLEDGMENTS

I would like to express my deepest gratitude to my advisor Assist. Prof. Dr. Hande Toffoli for her generous guidance and constant support combined with an encouraging, sincere, friendly attitude. I basically learned every tool I used in creating this thesis from her, through her ingenious and creative manners in sharing her scientific knowledge.

I also would like to thank deeply to my co-advisor Prof. Dr. Şinasi Ellialtıođlu for employing me in the project that this thesis is a part of, but mostly for his kind, insightful advisory.

I am sincerely thankful to Prof. Dr. Mehmet akmak and Assoc. Prof. Dr. Ersen Mete. They kindly provided me with valuable information pieces that were crucial for this thesis.

I want to thank to my project partners and friends Kıvılcım Bařak Vural and Murat Mesta for the very helpful and entertaining discussions. I thank to zge Akyar, Engin Torun and Trkan Kobak with whom I shared my office. I want to thank Murat Bektař, Nadir Ghazanfari, H. Mert Bozacı and all other friends for their support. A special thanks to Taylan Takan for patiently supporting and encouraging me any time I needed.

I owe infinitely many thanks to my dear mother for the unlimited love and support she offered.

This work is financially supported by TBİTAK, The Scientific and Technological Research Council of Turkey (Grant no: TBAG-107T560)

# TABLE OF CONTENTS

ABSTRACT . . . . .	iv
ÖZ . . . . .	v
ACKNOWLEDGMENTS . . . . .	vii
TABLE OF CONTENTS . . . . .	viii
LIST OF TABLES . . . . .	x
LIST OF FIGURES . . . . .	xii
CHAPTERS	
1 INTRODUCTION . . . . .	1
1.1 Theoretical Background on DFT . . . . .	2
1.1.1 Kohn–Sham Equations . . . . .	3
1.1.2 Exchange–Correlation Functionals . . . . .	5
1.1.3 Plane-wave Basis . . . . .	6
1.1.4 Pseudopotentials . . . . .	9
1.1.5 Self-Consistent Cycle . . . . .	10
1.2 Applications of TiO <sub>2</sub> Anatase Nanoforms . . . . .	11
2 STRUCTURAL PROPERTIES OF ANATASE NANOSHEETS AND NANOTUBES . . . . .	14
2.1 Bulk Calculations . . . . .	14
2.1.1 Band Gap Correction Using DFT+U . . . . .	16
2.2 Properties of Anatase Nanosheets Derived from the (001) Surface . . . . .	18
2.2.1 Bulk Constrained Relaxations . . . . .	19
2.2.2 Optimization of Isolated Sheets . . . . .	20
2.3 Lepidocrocite Structure . . . . .	21

2.3.1	O vacancy at Lepidocrocite . . . . .	23
2.4	Anatase Nanotubes . . . . .	25
3	GOLD ADSORPTION ON LEPIDOCROCITE NANOSHEETS . . . . .	28
3.1	Adsorption of Au Monomers . . . . .	29
3.1.1	Au <sub>1</sub> on the (1×1) Surface . . . . .	29
3.1.2	Au <sub>1</sub> on the (2×2) Surface . . . . .	30
3.2	Adsorption of Au Dimers . . . . .	32
3.3	Au <sub>1</sub> and Au <sub>2</sub> Adsorption at O Vacancy . . . . .	35
3.4	Adsorption of Au Trimers and Au Quatromers . . . . .	39
4	CONCLUSION . . . . .	44
	REFERENCES . . . . .	46

## LIST OF TABLES

### TABLES

Table 2.1 Computed equilibrium lattice parameters of TiO <sub>2</sub> anatase bulk structure using different methods: standard minimization (Std.), Parrinello-Rahman (PR) and Wentzchowitch (W) type variable-cell dynamics. The errors with respect to experimental values (Expt.) are indicated as percentage in parantheses. . . . .	15
Table 2.2 Calculated formation energies $E_{form}$ , surface energies $E_{surf}$ and band gaps ( $E_g$ ) of TiO <sub>2</sub> anatase (001) derived nanosheets labeled by the corresponding number of layers ( $N_l$ ) with lattice constants constrained to the bulk values . . . . .	20
Table 2.3 Lattice parameter ( $a$ ), formation energies ( $E_{form}$ ), surface energies ( $E_{surf}$ ) and band gaps ( $E_g$ ) of optimized (001)derived anatase nanosheets from 1 to 4 ML . . . . .	21
Table 2.4 Lattice parameters $a$ and $b$ , formation energy $E_{form}$ , surface energy $E_{surf}$ , Fermi level with respect to the valence band top $E_f$ and band gap $E_g$ for the lepidocrocite-type nanosheet. . . . .	22
Table 2.5 Structural parameters: distance between the inner bridging O atoms ( $d_{in}$ ) and outer ones ( $d_{out}$ ), inner ( $A_{in}$ ) and outer ( $A_{out}$ ) Ti-O-Ti angles with O being the non-bridging oxygen, formation energies ( $E_{form}$ ) and band gaps ( $E_g$ ) of the lepidocrocite nanotubes labeled by the corresponding diameter $D$ . . . . .	27
Table 3.1 Calculated binding energies ( $E_b$ ), Fermi levels ( $E_f$ ) relative to the valence-band top , and the distances that the Au atom makes with the surface O and Ti atoms for Au monomer adsorption models on a (2×2) surface. . . . .	32

Table 3.2 Calculated binding energies ( $E_b$ ), Fermi levels ( $E_f$ ) relative to the valence-band top, band gap values ( $E_g$ ) and the distances of adsorbed Au dimers . . . . . 35

## LIST OF FIGURES

### FIGURES

Figure 2.1	Band gap dependence of the TiO <sub>2</sub> bulk anatase on the U parameter at 30 and 40 Ryd cut-off values. . . . .	17
Figure 2.2	Band structures of bulk anatase calculated using (a) DFT and (b) DFT+U with U=7 eV at 40 Ryd. . . . .	18
Figure 2.3	Relaxed structures of the lepidocrocite nanosheet: (a) Side view along (100); (b) Side view along (010); (c) top view. . . . .	22
Figure 2.4	(a) The band structure and (b) the corresponding DOS/PDOS plot of the lepidocrocite nanosheet. . . . .	23
Figure 2.5	O vacancy on the (2×2) lepidocrocite sheet: (a) Side view of the relaxed structure along (100); (b) Band structure with corresponding DOS/PDOS. . . . .	24
Figure 2.6	Front (on the left) and side (on the right) views of the relaxed structures of TiO <sub>2</sub> lepidocrocite nanotubes rolled up along (010) with different diameters. There are 5 unit cells in the side views. . . . .	26
Figure 2.7	Band Structures of the lepidocrocite nanotubes of different <i>D</i> . . . . .	27
Figure 3.1	(1×1) adsorption of Au <sub>1</sub> : (a) Top view, (b) Band structure with DOS/PDOS. . . . .	29
Figure 3.2	(2×2) adsorption of Au <sub>1</sub> on O1: (a) Side view along (100); (b) Side view along (010) and (c) Band structure with DOS/PDOS . . . . .	32
Figure 3.3	(2×2) adsorption of Au <sub>1</sub> on Ti1: (a) Side view along (100); (b) Side view along (010) and (c) Band structure with DOS/PDOS. . . . .	33

Figure 3.4 (2×2) adsorption of Au <sub>1</sub> on O <sub>2</sub> on a single side [(a),(b) and (c)] and on both sides [(c),(d) and (e)]: (a),(d) Side view along (100); (b),(e) Side view along (010) and (c),(f) Band structure with DOS/PDOS. . . . .	34
Figure 3.5 (2×2) adsorption of Au <sub>1</sub> on O <sub>2</sub> : (a) Side view along (100), (b) Side view along (010) and (c) Band structure with DOS/PDOS. . . . .	35
Figure 3.6 (2×2) adsorption of Au <sub>2</sub> on O <sub>1</sub> : (a) Side view along (100); (b) Side view along (010) and (c) Band structure with DOS/PDOS. . . . .	36
Figure 3.7 (2×2) adsorption of Au <sub>2</sub> diagonally positioned on O <sub>1</sub> : (a) Side view along (100); (b) Side view along (010) and (c) Band structure with DOS/PDOS. . . . .	36
Figure 3.8 (2×2) adsorption of vertically oriented Au <sub>2</sub> on O <sub>2</sub> : (a) Side view along (100); (b) Side view along (010) and (c) Band structure with DOS/PDOS.	37
Figure 3.9 (2×2) adsorption of horizontal Au <sub>2</sub> on O <sub>2</sub> : (a) Top view; (b) Side view along (010) and (c) Band structure with DOS/PDOS. . . . .	37
Figure 3.10 (2×2) adsorption of Au <sub>1</sub> at O vacancy: (a) Side view along (100); (b) Side view along (010) and (c) Band structure with DOS/PDOS. . . . .	39
Figure 3.11 (2×2) adsorption of Au <sub>2</sub> at O vacancy: (a) Side view along (100); (b) Side view along (010); (c) Band structure with DOS/PDOS and (d) PDOS detail around the band gap. . . . .	40
Figure 3.12 Relaxed structures of triangular Au <sub>3</sub> forming a chain: (a) Top view, (b) Side view along (100) and (c) Band structure with DOS/PDOS. . . . .	41
Figure 3.13 (2×2) adsorption of Au <sub>3</sub> on O <sub>1</sub> : (a) Side view along (100), (b) Side view along (010) and (c) Band structure with DOS/PDOS. . . . .	41
Figure 3.14 (2×2) adsorption of Au <sub>4</sub> on O <sub>1</sub> : (a) Side view along (100); (b) Side view along (010); (c) Band structure with DOS/PDOS and (d) PDOS detail around the band gap. . . . .	43

# CHAPTER 1

## INTRODUCTION

Titanium dioxide ( $\text{TiO}_2$ ) which is a wide band-gap semiconductor acting as a photocatalyst, is extensively employed in various important applications such as dye-sensitized solar-cells [1], hydrogen production [2], self-cleaning coatings [3], gas sensing devices [4], water and air purification [5] and lithium batteries [6]. Promotion (in some cases, prevention) of the photocatalytic behaviour of  $\text{TiO}_2$  is of crucial importance for these applications. Although the underlying physical mechanisms of photocatalysis are not yet very well understood, numerous researches have shown that this can indeed be achieved either by modifying the size and shape of the involving  $\text{TiO}_2$  particles or through adsorption of various additional chemical species [7,8]. In this thesis we carry a comprehensive investigation on the structural and chemical properties of two-dimensional  $\text{TiO}_2$  anatase nanosheets and nanotubes derived from them, and also Au adsorption on the sheets via computer simulations using density functional theory (DFT).

In the first part of the thesis we present a brief overview of the theoretical basics of DFT. Starting from basic quantum mechanics, we provide a sketch of DFT formalism aiming at validating its suitability in describing nano structures whose novel characteristics arise largely from quantum confinement effects and also providing background information about the specific tools used. Additionally, we give some general information regarding the properties of  $\text{TiO}_2$  nano structures and photocatalysis processes.

The second part consists of structural calculations. We start from bulk properties and proceed to nanosheets with particular emphasis on the lepidocrocite-type nanosheet

structure. Finally, we investigate properties of anatase nanotubes formed by rolling lepidocrocite sheets.

The third part is mainly devoted to gold adsorption on lepidocrocite sheets. By systematically analysing various cases, we try to gain insight about the properties of Au interaction with lepidocrocite surface. We explore different adsorption sites for Au monomers and Au dimers and investigate their properties. Adsorption at the oxygen vacancy is also taken into consideration. We also studied adsorption of small Au clusters consisting of 3 and 4 atoms in order to inspect the variations in the band structures as a function of cluster size.

### 1.1 Theoretical Background on DFT

Investigation of the properties of nanometer scale materials demands a quantum treatment and in order to get a full quantum mechanical description of any system for the static case, one has to solve the time-independent Schrödinger equation:

$$\hat{H}\Psi = E\Psi . \quad (1.1)$$

For a many-body system consisting of electrons and nuclei, the wave function depends on the electronic and nuclear coordinates labeled as  $\mathbf{r}_i$  and  $\mathbf{R}_I$  respectively:

$$\Psi = \Psi(\mathbf{r}_i, \mathbf{R}_I) . \quad (1.2)$$

And the form of the corresponding non-relativistic Hamiltonian is:

$$\begin{aligned} \hat{H} = & -\frac{\hbar^2}{2m_e} \sum_i \nabla_i^2 + \frac{1}{4\pi\epsilon_0} \left( -\sum_{i,I} \frac{Z_I e^2}{|\mathbf{r}_i - \mathbf{R}_I|} + \frac{1}{2} \sum_{i \neq j} \frac{e^2}{|\mathbf{r}_i - \mathbf{r}_j|} \right) \\ & - \sum_I \frac{\hbar^2}{2M_I} \nabla_I^2 + \frac{1}{4\pi\epsilon_0} \frac{1}{2} \sum_{I \neq J} \frac{Z_I Z_J e^2}{|\mathbf{R}_I - \mathbf{R}_J|} \\ = & \hat{T} + \hat{V}_{ext} + \hat{V}_{int} + \hat{T}_I + E_{IJ} . \end{aligned} \quad (1.3)$$

Although the above formulation is straightforward, obtaining exact solutions especially for large systems is an impossible task. Firstly due to entangled states which

forbid the wave function to be separated into single-particle components, and secondly due to the immeasurable computational load such a task requires. Thus, several approximations are needed.

The first of these is the Born–Oppenheimer approximation [9,10] which allows the wave function to be broken into electronic and nuclear components. Basically, it states that the instantaneous electronic states are not affected by the motion of the much heavier nuclei. As the nuclear mass  $M_I$  becomes very large, the associated kinetic energy term,  $\hat{T}_I$ , can be ignored. Also, the nucleus–nucleus interaction term,  $E_{II}$ , only has a constant contribution which can be added afterwards.

Then the main problem at hand is to solve the Schrödinger equation for the electronic wave function  $\Psi_e(\mathbf{r}_i)$ , by using the Hamiltonian (in atomic units where  $\hbar = e = m_e = 4\pi\epsilon_0 = 1$ ):

$$\begin{aligned}\hat{H}_e &= -\frac{1}{2} \sum_i \nabla_i^2 - \sum_{i,I} \frac{Z_I}{|\mathbf{r}_i - \mathbf{R}_I|} + \frac{1}{2} \sum_{i \neq j} \frac{1}{|\mathbf{r}_i - \mathbf{r}_j|} \\ &= \hat{T} + \hat{V}_{ext} + \hat{V}_{int} .\end{aligned}\tag{1.4}$$

The nucleus–electron interaction, namely the external potential,  $\hat{V}_{ext}$ , is a classical Coulombic interaction, whereas the electron–electron interaction,  $\hat{V}_{int}$ , makes the wave function non–separable due to quantum mechanical exchange–correlation effects. Moreover, the dependence of  $\Psi_e(\mathbf{r}_i)$  on  $3N$  variables for an  $N$ -electron system still demands a vast computational capacity even for storage. This means that further approximations and different approaches are required for practical calculations. DFT is one of the most successful methods in providing fast and accurate computation of many-body systems along with Hartree–Fock and Quantum Monte Carlo methods.

### 1.1.1 Kohn–Sham Equations

The electronic Hamiltonian in equation (1.4) suggests that any many-body system is basically a collection of interacting electrons moving in an external potential. Early quantum statistical models such as the Thomas–Fermi theory [11,12] reasonably presumed that such a system could be analyzed using the density of electrons as the

central variable instead of the wave function. Although these failed to accurately describe real systems, DFT followed the same approach and emerged as an exact theory.

The electron density is the 3-dimensional function giving the probability of finding an electron at a particular location  $\mathbf{r}$  in space:

$$n(\mathbf{r}) = N \int |\Psi(\mathbf{r}_1, \mathbf{r}_2, \dots, \mathbf{r}_N)|^2 d\mathbf{r}_2 d\mathbf{r}_3 \dots d\mathbf{r}_N . \quad (1.5)$$

Clearly, the density is determined by the wave function as any other observable. The question is to demonstrate the reverse case. Indeed, it was proven by Hohenberg and Kohn [13] that the ground state wave function for a fixed external potential is a unique functional of the ground state density. They also showed that the energy corresponding to this ground state density acquires its minimum value which equals the ground state energy:

$$E_0 = \int V_{ext}(\mathbf{r})n(\mathbf{r})d\mathbf{r} + F[n(\mathbf{r})] . \quad (1.6)$$

In the above expression,  $F[n(\mathbf{r})]$  contains kinetic energy and electron–electron interaction terms. It is a universal functional as it is independent of the system in consideration.

In order to be able to use Hohenberg–Kohn theorems in practice for real calculations, Kohn and Sham [14] provided a way in which the density is written in terms of fictitious single particle orbitals:

$$n(\mathbf{r}) = \sum_i |\Phi_i(\mathbf{r})|^2 . \quad (1.7)$$

In essence, Kohn–Sham formalism assumes an auxiliary system of non-interacting electrons experiencing an effective potential,  $V_{eff}$ , which mimics not only the ionic potentials but the interactions with all other electrons as well.  $V_{eff}$  contains both the external potential and electron–electron interaction contributions. The latter is broken into two parts: the Hartree term describing the Coulombic repulsion for a non-interacting electron system, plus, the exchange–correlation potential,  $V_{xc}$ , for the effects arising from the interaction among electrons. Then  $V_{eff}$  in terms of density is:

$$V_{eff} = \int V_{ext}(\mathbf{r})n(\mathbf{r})d\mathbf{r} + \int \frac{n(\mathbf{r})n(\mathbf{r}')}{|\mathbf{r} - \mathbf{r}'|}d\mathbf{r}d\mathbf{r}' + V_{xc} . \quad (1.8)$$

These definitions of the density and the effective potential leads to single-particle Schrödinger like equations:

$$\hat{H}_{eff} = [\hat{T}' + \hat{V}_{eff}] \Phi_i(\mathbf{r}) = \epsilon_i \Phi_i(\mathbf{r}) . \quad (1.9)$$

The kinetic energy,  $\hat{T}'$ , in the Kohn–Sham Hamiltonian  $H_{eff}$ , is denoted by a prime as it is no longer the kinetic energy of the real system. A kinetic energy correction for the interacting case is included inside  $V_{xc}$  [22].

The Kohn–Sham equations has the peculiar characteristic that the  $V_{eff}$  depends on the density which already is the unknown parameter to be found. Eventually, they can only be solved by iterative calculations forming a self-consistent cycle, explained further in Section 1.1.5.

### 1.1.2 Exchange–Correlation Functionals

The exchange–correlation effects are due to the Pauli exclusion principle. The overlap of the anti-symmetric wave functions of interacting electrons results in an attractive or a repulsive effect apart from Coulombic forces. The complicated nature of the exchange-correlation energy  $E_{xc}$  prevents it to be expressible analytically in terms of the density. Thus, it is an approximated functional available in several different types each of which may work better in different systems. The most commonly used functionals are Local Density Approximation (LDA) and Generalized Gradient Approximation (GGA). Given  $E_{xc}$ , the corresponding potential  $V_{xc}$  used in Kohn-Sham equations is found by taking its functional derivative.

In constructing LDA functionals, it is assumed that locally, the density is homogeneous and the total exchange–correlation energy can be found by integrating the corresponding exchange–correlation energies:

$$E_{xc}^{LDA} = \int n(\mathbf{r})\epsilon_{xc}^{hom}(n(\mathbf{r}))d\mathbf{r} . \quad (1.10)$$

The homogeneous, local exchange-correlation energy,  $\epsilon_{xc}^{hom}$ , is obtained by adding the separately found exchange and correlation parts. The exchange and correlation energies are complicated as they are related to the whole system rather than pairwise interactions. Their determination is made by Quantum Monte Carlo simulations using different parameters. LDA types differ in this parametrization process and some of the most commonly used types are Perdew–Zunger (PZ) [15], Perdew–Wang (PW) [16].

GGA functionals attempt to improve LDA approach by including the gradient of the density in the integration:

$$E_{xc}^{GGA} = \int n(\mathbf{r})\epsilon_{xc}[n(\mathbf{r}), \nabla n(\mathbf{r})]d\mathbf{r} . \quad (1.11)$$

Most common GGA types are Becke–Lee–Yang–Parr (BLYP) [17,18] and Perdew–Burke–Ernzerhof (PBE) [19]. Although GGA not necessarily improves LDA it was proved to be more accurate in highly inhomogeneous systems. In this thesis we used GGA-PBE functionals as the homogeneity of the density is low in the systems we considered due to the surfaces on both sides of the sheets and existence of adsorbants.

### 1.1.3 Plane-wave Basis

To be able to numerically solve the Kohn–Sham equations (Eq. 1.9), the Kohn–Sham orbitals  $\Phi_i(\mathbf{r})$  should be expanded in terms of a finite basis set. The basis can be chosen as consisting of plane waves or localized orbitals. Localized orbitals are more appropriate in small, isolated systems such as atoms, molecules and nanoclusters. In this thesis, we performed all the calculations using the PWSCF software [20] which employs plane waves.

Using a plane wave basis requires working in the reciprocal space. The relation between the real space primitive vectors  $\mathbf{a}$  and the primitive reciprocal space vectors  $\mathbf{b}$  is:

$$\mathbf{a}_i \cdot \mathbf{b}_j = 2\pi\delta_{ij} . \quad (1.12)$$

The reciprocal unit cell defined by  $\mathbf{b}$  is the first Brillouin zone and the infinitely many vectors lying in this volume are denoted by  $\mathbf{k}$ . The vectors  $\mathbf{G}$  spanning the whole reciprocal space are defined as:

$$\mathbf{G}_m = m_i \mathbf{b}_i \quad (1.13)$$

where  $m$  is an integer.

Plane wave expansion of the Kohn–Sham orbitals is a direct result of the crystal structure. In a crystal as the ions are arranged regularly, the potential created by this system is periodic. According to Bloch’s Theorem [21], the wavefunction of particles placed in this potential will also be periodic with the same periodicity as the potential. It states that the eigenfunctions  $\Phi(\mathbf{r})$  of the Schrödinger equation for such a potential is the product of a cell-periodic function,  $u(\mathbf{r}, \mathbf{k})$  and a plane wave :

$$\Phi(\mathbf{r}) = u(\mathbf{r}, \mathbf{k}) \cdot e^{i(\mathbf{k}, \mathbf{r})} . \quad (1.14)$$

As any periodic function can be expanded in terms of plane waves,  $u(\mathbf{r}, \mathbf{k})$  can be written as:

$$u(\mathbf{r}, \mathbf{k}) = \frac{1}{\sqrt{\Omega}} \sum_{\mathbf{G}_m} c_i(\mathbf{k}, \mathbf{G}_m) e^{\mathbf{G}_m \cdot \mathbf{r}} \quad (1.15)$$

where  $\Omega$  is the volume of the unit cell and  $c_i(\mathbf{k}, \mathbf{G}_m)$  are the complex expansion coefficients.

Then the wavefunction of the system expanded in terms of plane waves is:

$$\begin{aligned} \Phi(\mathbf{r}) = \Phi_i(\mathbf{r}, \mathbf{k}) &= \frac{1}{\sqrt{\Omega}} \sum_{\mathbf{G}_m} c_i(\mathbf{k}, \mathbf{G}_m) e^{i(\mathbf{k} + \mathbf{G}_m) \cdot \mathbf{r}} \\ &= \sum_{\mathbf{G}_m} c_i(\mathbf{k}, \mathbf{G}_m) |\mathbf{k} + \mathbf{G}_m\rangle . \end{aligned} \quad (1.16)$$

For a given  $\mathbf{k}$ , the orthonormality property of the plane waves reads as:

$$\langle \mathbf{k} + \mathbf{G}_{m'} | \mathbf{k} + \mathbf{G}_m \rangle = \delta_{mm'} . \quad (1.17)$$

Using equations (1.16) and (1.17), the Kohn–Sham Hamiltonian (Eq. 1.9) can be written as:

$$\sum_{\mathbf{G}_m} \langle \mathbf{k} + \mathbf{G}_{m'} | \hat{H}_{eff} | \mathbf{k} + \mathbf{G}_m \rangle c_i(\mathbf{k}, \mathbf{G}_m) = \epsilon_i \sum_{\mathbf{G}_m} \delta_{mm'} c_i(\mathbf{k}, \mathbf{G}_m) = \epsilon_i \sum_{\mathbf{G}_m} c_i(\mathbf{k}, \mathbf{G}_{m'}) . \quad (1.18)$$

This matrix equation can be written compactly as:

$$\sum_{\mathbf{G}_m} H_{mm'} c_{i,m} = \epsilon_i \sum_{\mathbf{G}_m} c_{i,m'} . \quad (1.19)$$

Each operator forming the Hamiltonian should be considered separately. The kinetic energy operator is given by:

$$\langle \mathbf{k} + \mathbf{G}_{m'} | \hat{T} | \mathbf{k} + \mathbf{G}_m \rangle = - \langle \mathbf{k} + \mathbf{G}_{m'} | \frac{1}{2} \nabla^2 | \mathbf{k} + \mathbf{G}_m \rangle = \frac{1}{2} |\mathbf{k} + \mathbf{G}_m|^2 \delta_{mm'} . \quad (1.20)$$

The effective potential is periodic as stated before and it can be expanded as the wave function in Eq. (1.15) which actually is an inverse Fourier transformation:

$$V_{eff}(\mathbf{r}) = \frac{1}{\sqrt{\Omega}} \sum_{\mathbf{G}_m} V_{eff}(\mathbf{G}_m) e^{i(\mathbf{k}+\mathbf{G}_m)\cdot\mathbf{r}} . \quad (1.21)$$

The Fourier transformation from real to reciprocal space integrated over real space vectors is:

$$V_{eff}(\mathbf{G}) = \frac{1}{\sqrt{\Omega}} \int_{\mathbf{r}} V_{eff}(\mathbf{r}) e^{-i(\mathbf{k}+\mathbf{G}_m)\cdot\mathbf{r}} . \quad (1.22)$$

Combining equations (1.21) and (1.22), the effective potential matrix is given as:

$$\langle \mathbf{k} + \mathbf{G}_{m'} | V_{eff}(r) | \mathbf{k} + \mathbf{G}_m \rangle = \sum_{\mathbf{G}_m} V_{eff}(\mathbf{G}_m) \delta_{\mathbf{G}_m - \mathbf{G}'_m, \mathbf{G}_m} = V_{eff}(\mathbf{G}_m - \mathbf{G}_{m'}) . \quad (1.23)$$

Putting equations (1.18) and (1.22) together, the matrix elements of the Kohn–Sham Hamiltonian:

$$H_{mm'} = \frac{1}{2}|\mathbf{k} + \mathbf{G}_m|^2 \delta_{mm'} + V_{eff}(\mathbf{G}_m - \mathbf{G}_{m'}) . \quad (1.24)$$

The expansion requires summation over the infinitely many  $\mathbf{G}$ -vectors which is a computationally impossible task. However, for large  $\mathbf{G}$ , plane waves become negligible, thus the sum can be truncated at a certain value. This value is called the cut-off radius,  $E_{cut}$ , usually expressed in terms of kinetic energy in units of electronvolts or Rydbergs. Larger  $E_{cut}$  results in more accurate results but takes more computational time as the number of plane waves will increase accordingly. In order to determine the smallest possible  $E_{cut}$  value that gives accurate results, convergence tests should be conducted over a range of values.

Another approximation is the discretisation of the k-points set. Depending on the fact that the wavefunctions at the k-points that are very close to each other are almost identical, a certain region in the reciprocal space can be represented by a single k-point. Naturally, the denser the discrete k-points set is, the more accurate (but slower) the calculations will be. Different methods for the discretisation have been proposed and in this thesis we used the Monkhorst–Pack scheme [24]. Similar to the determination process of  $E_{cut}$ , the k-points grid should be subjected to convergence tests.

Lastly, as periodicity is essential for the plane wave basis, calculations are made over infinitely many periodic images of the considered unit cell extending in three dimensions even if the system does not have three dimensional periodicity. Thus, in performing plane wave calculations for finite systems, such a system should be placed inside a large enough supercell preventing the interaction between the periodic images.

#### 1.1.4 Pseudopotentials

Around regions close to the ions, the potential and hence the electronic wave function has a highly oscillating behaviour. Accurate representation of such a behaviour re-

quires a very large number of plane waves. The oscillations are mainly due to the core electrons and the part of the wave functions of the valence electrons around the ions oscillate as well due to orthogonality condition. After a certain radius, the wave function whose behaviour is determined by the valence electrons tend to become smooth which can be appropriately described by a few plane waves. Owing to the fact that almost any chemical and physical property of materials depends on the behavior of the valence electrons, the oscillatory core part is replaced by smoother pseudopotentials and as a result only the density of the valence electrons is considered in DFT calculations.

A pseudopotential generated for an atom should obey certain criteria in order to be accurate and transferable:

1. The pseudo wave function should overlap with the real wave function beyond a certain core radius,  $r_c$ .
2. The eigenvalues for a reference atomic configuration of the real and pseudo wave functions of the valence electrons should match.
3. The logarithmic derivatives of the real and pseudo wave functions should be equal at  $r_c$ .

A fourth criterion, called the norm-conservation condition [25] can also be counted which requires that the integrated charge inside  $r_c$  for the real and pseudo wave functions should agree. However this condition can be relaxed for the sake of obtaining smoother, hence computationally faster pseudopotentials. A widely employed class of pseudopotentials abandoning norm-conservation are ultrasoft pseudopotentials. In our calculations we used Vanderbilt type ultrasoft pseudopotentials [26] for each atom.

### 1.1.5 Self-Consistent Cycle

The iterative cycle needed to solve the Kohn–Sham equations is constructed as follows: starting from an initially guessed input density,  $n_{in}$ , the effective potential  $V_{eff}$  is calculated and fed to the Kohn–Sham equations. The Kohn–Sham Hamiltonian is

solved with this  $V_{eff}$  and the calculated new output density,  $n_{out}$ , is compared to  $n_{in}$ . If they are not consistent, the cycle repeats itself until self-consistency is achieved.

Rather than starting from a guessed density at the beginning of each cycle or directly feeding in the calculated output density, a mixture of the input and output densities is preferred for easier convergence. The simplest method is linear mixing formulated as:

$$n_{in}^{i+1} = \beta n_{out}^i + (1 - \beta)n_{in}^i = n_{in}^i + \beta(n_{out}^i - n_{in}^i) \quad (1.25)$$

where  $i$  denotes the  $i^{th}$  cycle and  $\beta$  is a number between 0 and 1. Different mixing schemes providing faster convergence have been proposed. A commonly used scheme is Broyden mixing [27] which we used for the bulk calculations in this thesis.

Most of the computational effort in the self-consistent cycle is spent to the solution of the Kohn–Sham equations expanded in a plane wave basis. The calculations require diagonalisation of very large matrices which makes direct diagonalisation too expensive. Different algorithms have been proposed for faster diagonalisation. In this thesis we used the Davidson algorithm [28].

## 1.2 Applications of TiO<sub>2</sub> Anatase NanofORMS

The photocatalytic properties of the TiO<sub>2</sub> have been discovered in the 1970's [29] and since then it constitutes to be an active research area. Photocatalysis occurs when an electron at the valence band of a semiconductor is excited by an incident photon having an energy equal to or larger than the band gap. The excited electron jumps to the conduction band while leaving a hole at the valence band. This electron-hole pair which can move through the lattice usually recombines by releasing heat, but if the excited electron can be trapped, it can be transferred to the molecules around the photocatalytic substrate to initiate reduction or oxidation reactions. The efficiency of a photocatalyst is measured by the number of initiated reactions per incident photon. Ideally, this ratio should be 1 (100%), but in most real-life systems this value is much smaller and its improvement is at the focus of the researches on photocatalysis.

The efficiency of TiO<sub>2</sub> based photocatalytic materials is improved by doping with impurities and/or by increasing the surface area that is exposed to photons by using

smaller TiO<sub>2</sub> substrates. Each procedure increase the number of electron-hole traps and hence the recombination rate reduces. Effects on photocatalytic activity of different dopants and of topological variations is extensively studied. Another drawback of TiO<sub>2</sub> is that by having a wide band gap, it is only sensitive to photons having energies in the ultraviolet (UV) region of the spectrum which makes only 3% of the suns radiation. Shifting the sensitivity towards the visible spectrum by narrowing the band gap is another major objective.

TiO<sub>2</sub> anatase is one of the most abundant polymorphs of TiO<sub>2</sub> among rutile and brookite. Although anatase is less stable than rutile which is the most common phase, it is considered to be more efficient in terms of photocatalytic activity [30]. The Degussa P-25 samples which are the standard commercial TiO<sub>2</sub> powders used in photocatalytic reactions, consist mainly (about 75%) of particles having anatase form [31].

Enhanced photocatalytic activity through usage of nanosized TiO<sub>2</sub> structures is mainly attributed to their large surface to volume ratio and quantum confinement effects. TiO<sub>2</sub> nanosheets and other nano structures derived from them are recently produced materials in this class. Nanosheets of anatase have been obtained by two experimental techniques: top-down approach consisting of exfoliation of layers from anatase crystals by soft-chemical processes [33,34] and bottom-up assembly from Ti and O<sub>2</sub> by electron-beam deposition onto a substrate such as Pt [35,36]. The most common technique is exfoliation which usually starts from commercial anatase powders and ends up with numerous randomly oriented nanosheet units (also called nanowhiskers) having various impurities and defects. Their characterization at the atomic scale is an intricate task but most experiments point at a lepidocrocite type structure possessing similar properties as the anatase (001) surface. Moreover, anatase nanotubes obtained via similar soft-chemical procedures also have a lepidocrocite form while some claiming their structure is that of a two-layered sheet delaminated from the (001) surface [37]. Another instance that relates the experimentally obtained nanosheets to the (001) surface is previous DFT studies showing that a lepidocrocite type sheet can be obtained directly from a two-layered (001) derived nanosheet via variable-cell relaxations [38].

TiO<sub>2</sub> nanotubes have the potential to be used in more efficient catalysis processes as recent researches have shown [39,40]. They are usually obtained from anatase nanoparticles by exposing them to soft-chemical processes as in the synthesis of nanosheets [41]. Although the exact formation mechanism of the nanotubes is still debated, the accepted theory is that by introducing water resolved ionic chemicals like NaOH, anatase particles separate into sheets and those sheets roll up in order to decrease their surface energy [42]. Nanotubes formed by using this procedure are multilayered with inner diameters of 5 to 10 nm and an interlayer separation of about 1 nm [37,41,42]. Another range of nanotubes produced by different processes are highly ordered large nanotube arrays formed on a metal substrate. These nanotube arrays consist of less crystallized tubes having much larger diameters ranging from 100 to 300 nm [43].

Another interesting case in TiO<sub>2</sub> catalysis processes is the improved photocatalytic efficiency through adsorption of chemically inert metals such as platinum and gold. It was shown that Au clusters deposited onto TiO<sub>2</sub> surfaces facilitate oxidation of some organic compounds, especially carbon monoxide (CO) with high efficiencies [53,54]. The size of the Au clusters resulting in highest CO oxidation rates is about 3 nm [55]. Additionally, an Au/TiO<sub>2</sub> based solar cell device have been modelled [56].

## CHAPTER 2

# STRUCTURAL PROPERTIES OF ANATASE NANOSHEETS AND NANOTUBES

In this chapter, we explore the properties of several anatase nanoforms. Firstly, we conduct convergence studies on the bulk anatase which is an essential part in testing the accuracy of the parameters used in any DFT calculation. We attempt to correct the band gaps which are consistently underestimated in standard GGA calculations by applying DFT+U method. Then we explore the bulk constrained properties and optimized structures of nanosheets derived from the (001) surface of anatase. A particular emphasis is given to the lepidocrocite-type nanosheets which is the experimentally observed structure. For this structure, we also examine the system with an oxygen vacancy. Finally, we investigate properties of nanotubes of different radii formed by rolling up lepidocrocite type sheets.

### 2.1 Bulk Calculations

Anatase has a tetragonal unit cell with lattice parameters  $a=3.782 \text{ \AA}$  and  $c=9.502 \text{ \AA}$  [44]. Each Ti atom in the anatase bulk is bonded to 6 O atoms and each O atom makes 3 Ti bonds. The Ti octahedron is distorted with the two axial Ti–O bonds longer than the four equatorial ones. The axial and equatorial Ti–O distances are  $1.95 \text{ \AA}$  and  $1.92 \text{ \AA}$  respectively, and the O–O distance is  $2.43 \text{ \AA}$ . The primitive cell of anatase contains two  $\text{TiO}_2$  units.

In our calculations we used ultrasoft GGA-PBE pseudopotentials as indicated in Section 2 of Chapter 1. Previous ab initio studies comparing different pseudopotentials

confirm that on the overall PBE gives more reliable results for the anatase structure [45]. We used a Gaussian type smearing of 0.02 Ryd, set the self-consistent energy error threshold to  $10^{-8}$  and after conducting convergence tests over a range of values we found that a kinetic energy cut-off of 30 Ryd and a  $(5 \times 5 \times 2)$  k-points mesh meet our purposes. As the unit cell is tetragonal, we determined the lattice parameters by interpolating the computed energies over varying  $a$  and  $c$  values for fixed volumes. Although not typically used for the determination of lattice parameters, another method for determining the equilibrium structure is to conduct variable-cell (VC) relaxations. Parinello–Rahman [46] and Wentzchovitch [47] type VC dynamics are available in the PWSCF package. We present the results found both by regular fitting process and by VC-relaxation in Table 2.1.

Table 2.1: Computed equilibrium lattice parameters of  $\text{TiO}_2$  anatase bulk structure using different methods: standard minimization (Std.), Parrinello-Rahman (PR) and Wentzchowitch (W) type variable-cell dynamics. The errors with respect to experimental values (Expt.) are indicated as percentage in parantheses.

Method	$E_{cut}$ [Ryd]	$a$ [Å]	$c$ [Å]
Std.	30	3.789 (0.19%)	9.520 (0.19%)
PR	30	3.795 (0.34%)	9.652 (1.58%)
PR	40	3.790 (0.21%)	9.650 (1.56%)
W	30	3.793 (0.29%)	9.645 (1.50%)
W	40	3.789 (0.19%)	9.603 (1.06%)
Expt.		3.782	9.502

Ideally, VC-relaxation eliminates the requirement to conduct standard relaxation many times for different lattice parameters. However, as our results indicate, VC-relaxation requires higher cut-off values for accurate results. Wentzchowitch type VC dynamics at 40 Ryd gave the best VC values with errors for both parameters lying within the acceptable error range (1%) for ab initio calculations. However, this method requires more iteration steps than Parrinello–Rahman dynamics, hence takes more time for convergence and is more dependent on  $E_{cut}$ . Moreover, the error for the  $c$  parameter is still 5 times larger than the one found by the regular fitting procedure. Thus we used the lattice parameters found from standard methods in calculating the band structure of bulk anatase and in the following calculations whenever necessary.

### 2.1.1 Band Gap Correction Using DFT+U

Anatase has an indirect band gap of 3.2 eV corresponding to a wavelength of 388 nm which lies in the UV range. Our calculated band gap is 2.08 eV which corresponds to an error of 35%. It is well known that GGA and LDA calculations may underestimate the band gaps of semiconductors with errors up to 50%. In many occasions, the shapes of the bands are more important and the band structures of similar systems are calculated with the same computational parameters, hence giving the same errors. They are then compared with each other. However, appropriate band gap corrections would lead to more realistic simulations especially for applications involving electronic excitations depending on the value of the band gap such as photocatalytic activity. A method used in correcting the band gaps is the DFT+U formalism. DFT+U method has proven its ability by giving improved band structures for Mott insulators consistently predicted as metals in standard DFT calculations [48]. Within our framework, previous studies on the TiO<sub>2</sub> rutile structure employing the DFT+U method, showed that the band gaps can be corrected by using an appropriate U parameter [49].

Basically, DFT+U imposes a Coulombic type additional functional for correct representation of the localized d orbitals of transition metals:

$$E'_{xc} = E_{xc} + E_U \quad (2.1)$$

$E_U$  is defined as:

$$E_U = U \frac{1}{2} \sum_{i \neq j} n_i n_j \quad (2.2)$$

where U is the number called the Hubbard U parameter in units of energy and  $n_i, n_j$  are occupation numbers. The determination of the appropriate U parameter for a given atom at a given site requires various tests and calculations for sensitive results even when using a simplified model as implemented in PWSCF [48]. However as our sole aim is to correct the band gap, we computed the gaps by assigning the same U value for each Ti atom in the unit cell. We conducted the calculations over integer U values ranging from 1 to 12 eV. We also tested the cut-off dependence of the U parameter by repeating the calculations at 40 Ryd. We concluded that the band gap increases by increasing U until a certain point, then starts to decrease, consistent with the previous results on rutile models. The band gap versus U dependence is shown in Figure 2.1.

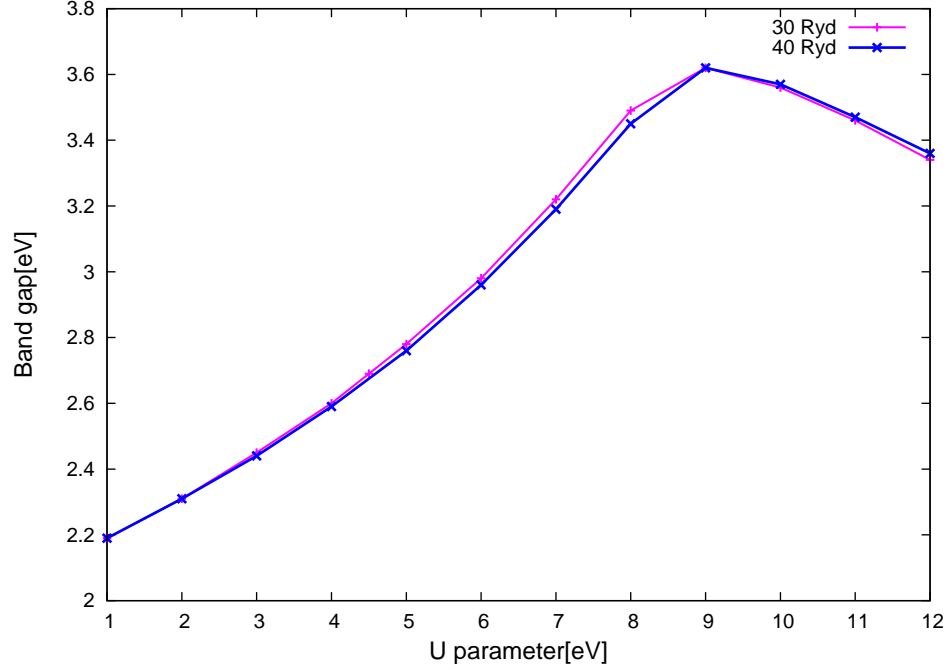


Figure 2.1: Band gap dependence of the  $\text{TiO}_2$  bulk anatase on the U parameter at 30 and 40 Ryd cut-off values.

We also inferred that the DFT+U correction has a slight dependence on the cut-off. At larger cut-off, the dependence is smoother and the slope is slightly smaller. At the maximum point of each cut-off, the band gap exceeded the experimental value. The U value that gives a band gap that is closest to the experiment is 7 eV which resulted in a gap of 3.22 eV for 30 Ryd and 3.19 eV for 40 Ryd. In order to monitor the effect of the U parameter on the shapes of the bands, we calculated the band structure of the anatase unit cell using  $U=7$  eV at 40 Ryd. The bands plotted with and without using DFT+U is presented in Figure 2.2. DFT+U mostly affected the conduction bands which mainly consist of states coming from the Ti 3d electrons. It visibly lessened the dispersion. Especially the bands around the  $\Gamma$  points are significantly shifted upwards.

In order to gain an insight about the effect of the U parameter on the structure of the unit cell, we run a PR type VC relaxation over the bulk unit in DFT+U formalism. At 30 Ryd cut-off, we set the U parameter to 7 eV which gave the band gap of 3.22 eV which is very close to the experimental value. We obtained  $a=3.89$  Å (an error of 2.85%) and  $c=9.75$  Å (an error of 2.61%). Although the errors with respect

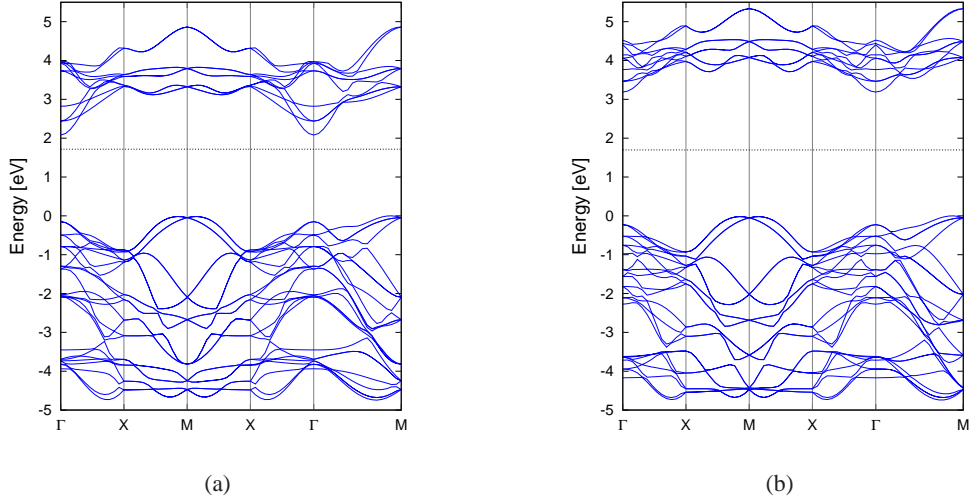


Figure 2.2: Band structures of bulk anatase calculated using (a) DFT and (b) DFT+U with  $U=7$  eV at 40 Ryd.

to experimental parameters are higher than those obtained from standard DFT runs, they are not too high indicating that DFT+U calculations may give accurate structural parameters as well as corrected band gaps.

## 2.2 Properties of Anatase Nanosheets Derived from the (001) Surface

Among the low index surfaces of anatase, the thermodynamically most stable surface is the (101) facet. Although the (001) surface is less stable, a layered structure manifests itself more clearly than other anatase surfaces. It is somewhat structurally similar to graphite. A systematic study comparing the photocatalytic activities of different anatase surfaces does not exist yet, but the (001) facet have been shown to be present in commercial powders along with (101), (100) and (010) planes [32]. The unreconstructed (001) surface consists of fivefold coordinated Ti atoms ( $Ti_{5c}$ ) with twofold coordinated bridging O atoms ( $O_{2c}$ ) and also threefold coordinated O atoms ( $O_{3c}$ ).

In this section we considered nanolayers stripped off from the anatase (001) surface which have thicknesses ranging from 1 to 6 monolayers (ML). First, we relax the structures with lattice parameters constrained to the previously obtained bulk values,

i.e.,  $a=3.789$ . Then we perform geometrical optimization to explore their isolated ground state structures by spanning the square lattice space.

Due to the irrelevancy of the total energies, we defined the sheet formation energy,  $E_{form}$ , as a parameter indicating the stability of the nanosheets with respect to the bulk form: where  $E_{sheet}/n$  is the total energy of the sheet divided by the number,  $n$ , of  $\text{TiO}_2$  units in the unit cell and  $E_{bulk}$  is the total energy of the bulk anatase per unit  $\text{TiO}_2$ :

$$E_{form} = E_{sheet}/n - E_{bulk} \quad (2.3)$$

where  $E_{sheet}/n$  is the total energy of the sheet divided by the number,  $n$ , of  $\text{TiO}_2$  units in the unit cell and  $E_{bulk}$  is the total energy of the bulk anatase per unit  $\text{TiO}_2$ . Additionally, as the sheets consist of surfaces of area  $A$  on the both sides, we also defined the surface energy,  $E_{surf}$  (in units of  $\text{J}/\text{m}^2$ ) as:

$$E_{surf} = [E_{sheet} - n \cdot E_{bulk}] / 2A \quad (2.4)$$

### 2.2.1 Bulk Constrained Relaxations

The computational parameters used in bulk constrained relaxations are identical to those of the bulk anatase for consistency. GGA-PBE ultrasoft pseudopotentials, Gaussian type smearing of 0.02 Ryd, 30 Ryd of cut-off energy and  $(5 \times 5 \times 1)$  k-points grid are used. Except that we use a local Thomas–Fermi mixing scheme [50] which is more appropriate for highly inhomogeneous systems containing surfaces. The consecutive slabs are at least 10 Å farther apart to prevent any interaction.

The computed results are summarized in Table 2.2. As expected,  $E_{form}$  of the sheets, gradually decreased by increasing the number of layers. This is an expected result as the nanosheets converge to the (001) surface by increasing number of layers. The least favored structure having the highest  $E_{form}$  is the 1 ML sheet which solely consists of  $\text{Ti}_{4c}$  and  $\text{O}_{2c}$  atoms. As  $\text{Ti}_{4c}$  atoms become  $\text{Ti}_{5c}$  in 2 ML sheets,  $E_{form}$  drops by one half. In thicker nanosheets,  $\text{Ti}_{6c}$  atoms starts to form below the surfaces and  $E_{form}$  gradually decreases. All the computed quantities for the 5 and 6 ML sheets are almost

equal.

Table 2.2: Calculated formation energies  $E_{form}$ , surface energies  $E_{surf}$  and band gaps ( $E_g$ ) of TiO<sub>2</sub> anatase (001) derived nanosheets labeled by the corresponding number of layers ( $N_l$ ) with lattice constants constrained to the bulk values

$N_l$	$E_{form}$ [eV]	$E_{surf}$ [J/m <sup>2</sup> ]	$E_g$ [eV]
1	2.10	1.17	1.97
2	0.85	0.95	2.20
3	0.53	0.89	2.22
4	0.39	0.88	2.04
5	0.31	0.87	1.93
6	0.26	0.87	1.93

The surface energy drops by increasing thickness and is fixed at 5 ML. The value of 0.87 J/m<sup>2</sup> is close to that of the (001) previously calculated as 0.90 J/m<sup>2</sup> [30]. In the band gaps we do not observe a direct dependence on the number of layers. From 1 to 3 ML the gap increases and then drops again.

### 2.2.2 Optimization of Isolated Sheets

We investigated the optimized structures of isolated nanosheets by following a basic fitting procedure consisting of spanning the square lattice space within  $\pm 25\%$  of the bulk value. We considered nanosheets of only 1 to 4 layers thick as they are expected to show greatest deviation from the bulk structure due to their decreased size. Due to the lack of experimental data, rigorous investigation of the global structural minimum of the sheets may require the span of a much larger and tetragonal space. Previous ab-initio studies on anatase nanosheets used VC relaxation techniques to this end and concluded that (001) derived sheets having an odd-number of layers indeed assume tetragonal unit cells [38]. However, they stated that these structures may not be the global-minimum structures. Our experience with VC dynamics for anatase structures proved that it is an expensive procedure requiring large cut-off energies and low mixing-beta values for convergence and yet easily stops at a nearby local minimum. Thus, without claiming to find the minimum structures, we report the results of the square-fitting calculations, resumed in Table 2.3.

The layers tend to shrink as the thickness decreases. As the size of the unit cell

Table 2.3: Lattice parameter ( $a$ ), formation energies ( $E_{form}$ ), surface energies ( $E_{surf}$ ) and band gaps ( $E_g$ ) of optimized (001)derived anatase nanosheets from 1 to 4 ML

$N_l$	$a$ [Å]	$E_{form}$ [eV]	$E_{surf}$ [J/m <sup>2</sup> ]	$E_g$ [eV]
1	3.185	0.62	1.17	3.51
2	3.520	0.65	0.95	2.72
3	3.661	0.50	0.89	2.12
4	3.709	0.37	0.88	2.21

reduces, the formation energy drops. The change in  $E_{form}$  relative to the bulk constrained calculations is most evident in the 1 ML sheet whose  $E_{form}$  decreased by more than one third.  $E_{form}$  of the 2 ML is lower by 0.2 eV while those of the 3 and 4 ML sheets are only slightly lower than their bulk counterparts. The 1 ML sheet has a fairly large band gap, the widest of any structure considered throughout this thesis. The band gap of the 2 and the 4 ML sheet widened while the gap of the 3 ML sheet narrowed. The variation in the gaps relative to the number of layers is the reverse of the bulk constrained trend. The gap decreases from 1 to 3 layers and widens again at 4 ML.

### 2.3 Lepidocrocite Structure

The lepidocrocite structure is shown in Fig. 2.3. We used the *Xcrysden* software for crystal structure displays [51]. The relation of the lepidocrocite-type structure to the (001) derived nanosheets is that it can be obtained by sliding the upper layer of a 2 ML sheet by half a unit cell in the (100) direction. Contrary to anatase nanosheets it has a rectangular unit cell with lattice parameters  $a=3.02$  Å along (100) and  $b=3.73$  Å along (010). As the upper layer of the 2 ML sheet is slided, all the Ti atoms become sixfold coordinated instead of five and the unit cell shrinks significantly along (100). The bridging oxygens remain twofold coordinated while the non-bridging oxygens become fourfold coordinated. Ti-O bond length with the two bridging O is 1.83 Å, and with the non-bridging O atoms it is 1.96 Å along (100) and 2.22 Å along (010). Ti-O-Ti angle for bridging O is 112°, for nonbridging O it is 86° in the (100) direction and 144° in the (010) direction. The thickness of the lepidocrocite sheet measured from bridging O atoms on opposing sides is 4.3 Å.

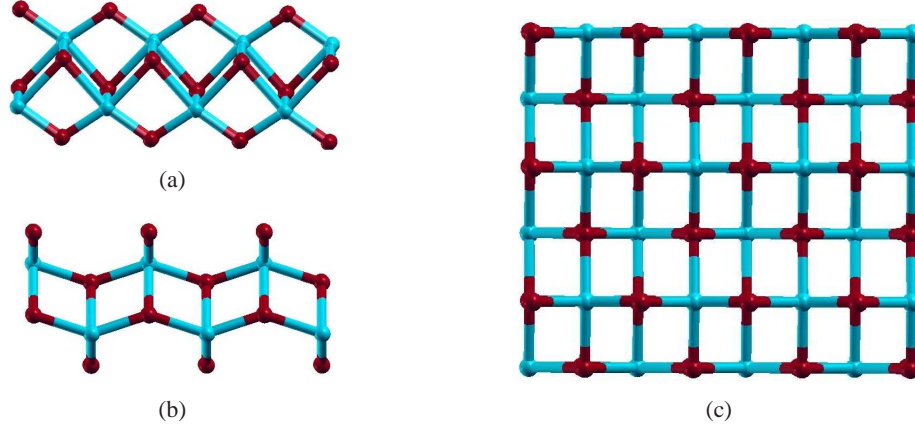


Figure 2.3: Relaxed structures of the lepidocrocite nanosheet: (a) Side view along (100); (b) Side view along (010); (c) top view.

Occurrences of  $Ti_{6c}$  as in the bulk anatase, significantly lowers the formation energy of the lepidocrocite sheet relative to other nanosheets indicating much higher stability. It is only 0.15 eV higher than the bulk phase. This data is a confirmation of the experimental results that in the synthesis of anatase nanosheets a lepidocrocite structure is favored. Surface energy is also low, even lower than the surface energy of the (001) surface. The calculated properties for the lepidocrocite sheet are presented in Table 2.4.

Table 2.4: Lattice parameters  $a$  and  $b$ , formation energy  $E_{form}$ , surface energy  $E_{surf}$ , Fermi level with respect to the valence band top  $E_f$  and band gap  $E_g$  for the lepidocrocite-type nanosheet.

$a$ [ $\text{\AA}$ ]	$b$ [ $\text{\AA}$ ]	$E_{form}$ [eV]	$E_{surf}$ [ $\text{J/m}^2$ ]	$E_f$ [eV]	$E_g$ [eV]
3.02	3.73	0.15	0.41	1.75	3.03

The band structure and the density of states (DOS) with the projected density of states (PDOS) plots are shown in Figure 2.4. As the bulk anatase, the conduction band consists mainly of the Ti 3d orbitals and the valence band is originating from O 2p orbitals. Lepidocrocite nanosheet has a band gap of 3.03 eV which is wider than the other sheets except the optimized 1 ML sheet. The band gap is indirect as the conduction band minimum is situated around X while the valence band maximum is at the  $\Gamma$  point. DFT+U calculations for lepidocrocite performed at an  $E_{cut}$  of 40

Ryd gave similar shapes to those for the bulk anatase. The band gap widened until it reaches a value of 4.09 eV at  $U=8$  eV and the gap opening ceased afterwards. This means that a real band gap of about 4 eV which corresponds to about 310 nm is not unlikely for anatase lepidocrocite structures. This result in accordance with the experimental observations that the optical spectrum of anatase nanosheets is considerably blue shifted relative to the bulk [52].

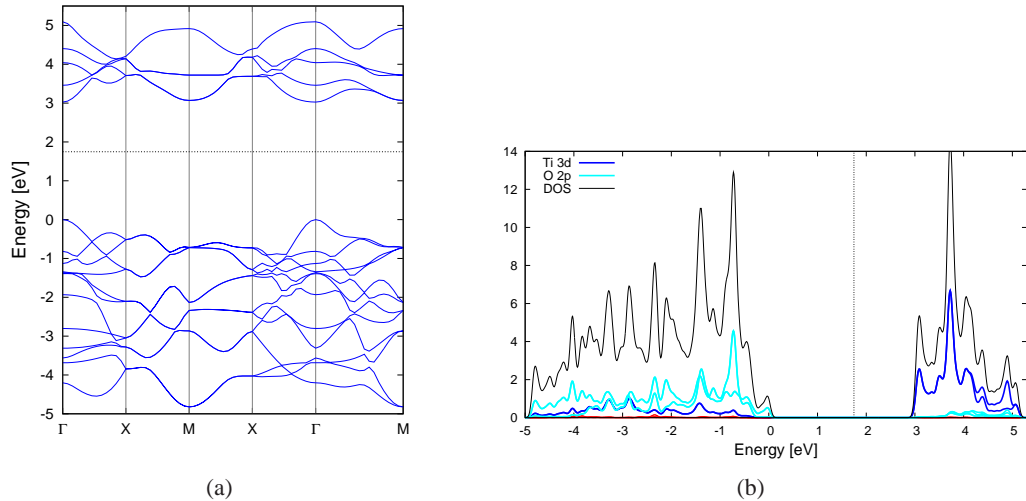


Figure 2.4: (a) The band structure and (b) the corresponding DOS/PDOS plot of the lepidocrocite nanosheet.

### 2.3.1 O vacancy at Lepidocrocite

Many real-life materials used in experiments have surface deficiencies and oxygen vacancies at anatase surfaces is very common. They play an important role in catalysis processes as many adsorbants prefer these vacancy sites and they also have an important role in creating electron-hole traps. Oxygen vacancies are either already present on the surfaces by a few percent or they can be created by electron bombardment [58]. Evidence of O defects on the lepidocrocite structures originates from researches on anatase nanotubes. Studies showed that the synthesized lepidocrocite tubes have oxygen vacancy concentrations of approximately 20% [29]. In this section we examined the case with a single oxygen vacancy per  $(2 \times 2)$  cell which corresponds

to a vacancy concentration of 25%.

We created the structure simply by ripping off one bridging O from the (2×2) lepidocrocite surface. We used the same computational parameters as in nanosheets calculations. The relaxed O defected structure is shown in Figure 2.5. Upon relaxation the two Ti atoms become fivefold coordinated and they moved farther apart from each other. The Ti-Ti distance along (100) at the vacancy increased by 0.17 Å and obtained a value of 3.19 Å and the Ti-Ti distance under the bridging O atom near the vacancy is 2.85 Å.

We defined a vacancy formation energy,  $E_{vform}$  as:

$$E_{vform} = E_{sheet} - (E_{vac} + \frac{1}{2}E_{O_2}) \quad (2.5)$$

where  $E_{sheet}$  is the total energy of the clean lepidocrocite sheet,  $E_{vac}$  is the energy of the vacancy and  $E_{O_2}$  is the energy of an oxygen molecule. We computed this energy to be 6.21 eV.

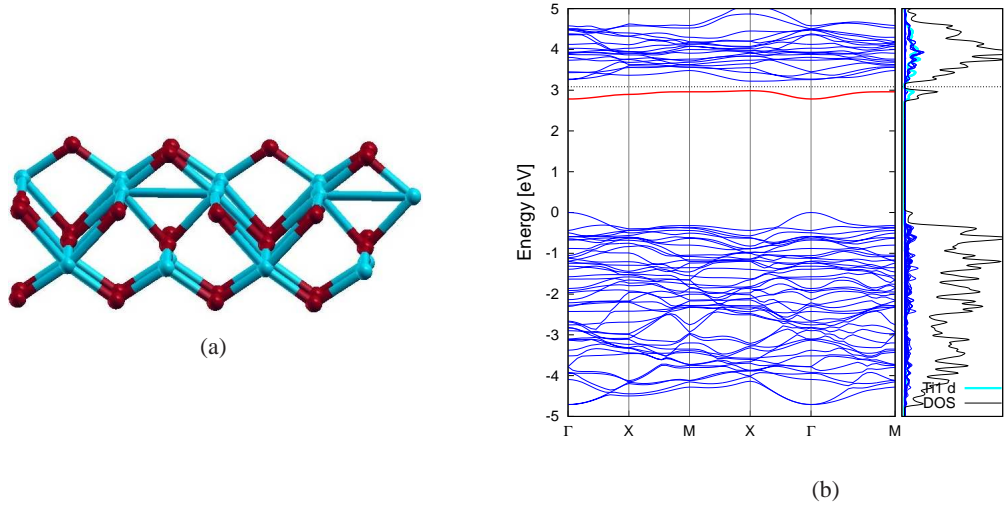


Figure 2.5: O vacancy on the (2×2) lepidocrocite sheet: (a) Side view of the relaxed structure along (100); (b) Band structure with corresponding DOS/PDOS.

As seen from the band structure (Fig. 2.5), a single defect site (colored in red) exists inside the band gap, located just below the conduction band. The Fermi level is situated between this impurity site and the conduction band minimum indicating a semiconductor system. However, it should be noted that the band gap value which is 0.23 eV is so small that it is comparable to the smearing. As depicted from the PDOS,

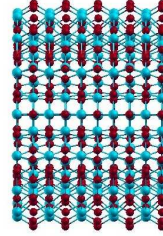
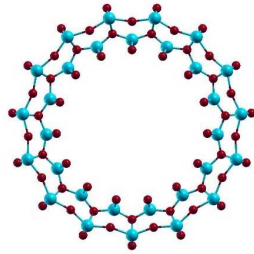
this state mainly consists of d orbitals of the  $Ti_{5c}$  atoms located near the vacancy. The 4s orbitals of the same Ti atoms has some contribution also. In Chapter 3, Au monomer and Au dimer adsorption at this vacancy site will be investigated.

## 2.4 Anatase Nanotubes

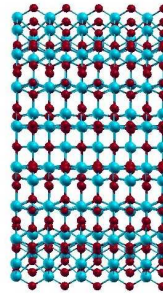
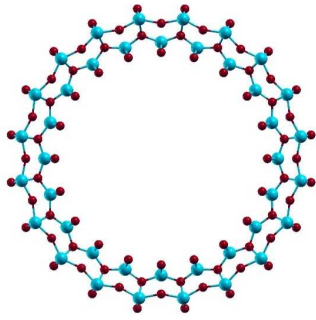
In this section we investigated properties of nanotubes generated from lepidocrocite type nanosheets. Due to the large dimensions of the anatase nanotubes synthesized in laboratories as mentioned in Chapter 1, it is difficult to simulate these real-life tubes using DFT considering the computational load. However, examination of smaller tubes as we attempt in this section, may give valuable information. Besides, for sufficiently large real-life nanotubes, the curvatures and interatomic interactions between walls of the tubes are negligible for simulation purposes. Hence, much of the information obtained from flat sheets would be valid for them as well.

As in carbon nanotubes formed from graphene sheets, lepidocrocite sheets can be rolled into tubes in an infinitely many ways. However, in accordance with the results of experiments and with previous theoretical work on anatase nanotubes [40], the curvature of our tubes is in the (010) direction. We examined three models having different diameters whose relaxed structures are shown in Figure 2.6. The inner and the outer sides of the tubes are covered with monolayers of bridging oxygens. The inner diameters of the considered tubes are 15 Å (1.5 nm), 20 Å (2.0 nm) and 26 Å (2.6 nm). Our experience with smaller tubes having the same structure demonstrated that they are not stable below a certain diameter. The tubes have 90, 120 and 150 atoms in their unit cells respectively. Due to the curvature, the inner and the outer surfaces are not symmetric. As seen from Figure 2.6, in all the tubes, the bond between the Ti atom on the inner side and the non-bridging O atom on the outer side is broken. Hence, these Ti atoms are four-fold coordinated while the outer Ti remain six-fold coordinated. Under coordinated Ti atoms decreases the stability with respect to the flat lepidocrocite sheet and this configuration results in higher formation energies.

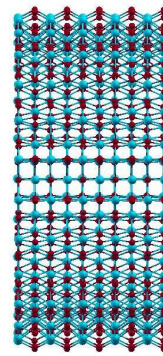
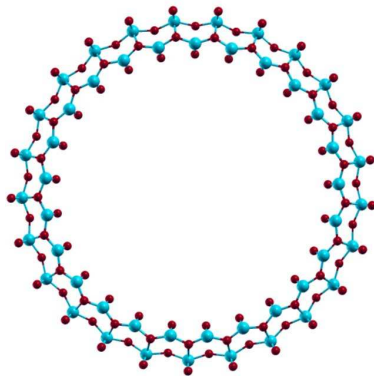
The formation energies are calculated from Eq. (2.3).  $E_{form}$  is lowered by increasing the diameter. This means that larger tubes are more stable.  $E_{form}$  of the largest tube



(a)  $D=1.5$  nm



(b)  $D= 2.0$  nm



(c)  $D= 2.6$  nm

Figure 2.6: Front (on the left) and side (on the right) views of the relaxed structures of  $\text{TiO}_2$  lepidocrocite nanotubes rolled up along (010) with different diameters. There are 5 unit cells in the side views.

is about 2 times higher than the lepidocrocite sheet. The structural parameters and the computed quantities of the relaxed structures are resumed in Table 2.5.

Table 2.5: Structural parameters: distance between the inner bridging O atoms ( $d_{in}$ ) and outer ones ( $d_{out}$ ), inner ( $A_{in}$ ) and outer ( $A_{out}$ ) Ti-O-Ti angles with O being the non-bridging oxygen, formation energies ( $E_{form}$ ) and band gaps ( $E_g$ ) of the lepidocrocite nanotubes labeled by the corresponding diameter  $D$ .

	$D= 1.5$ nm	$D= 2.0$ nm	$D= 2.6$ nm
$d_{in}(\text{O-O}) [\text{\AA}]$	2.93	3.04	3.26
$d_{out}(\text{O-O})[\text{\AA}]$	4.64	4.35	4.32
$A_{in}(\text{Ti-O-Ti})$	$123^\circ$	$125^\circ$	$131^\circ$
$A_{out}(\text{Ti-O-Ti})$	$164^\circ$	$159^\circ$	$157^\circ$
$E_{form}$ [eV]	0.67	0.48	0.32
$E_g$ [eV]	2.39	2.44	2.71

The band structures of the nanotubes plotted along  $\Gamma X$  are shown in Figure 2.7. The band gap increased with increasing size, yet it is smaller than the flat lepidocrocite sheet in all three cases. Each tube has an indirect band gap as the lepidocrocite sheet with the valence band maximum located at the  $\Gamma$  point the conduction band minimum located at X.

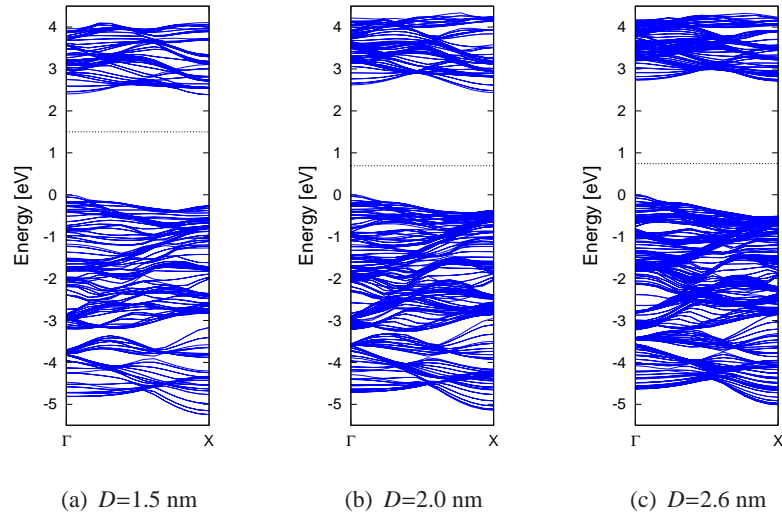


Figure 2.7: Band Structures of the lepidocrocite nanotubes of different  $D$ .

## CHAPTER 3

### GOLD ADSORPTION ON LEPIDOCROCITE NANOSHEETS

In this chapter adsorption of Au monomer ( $\text{Au}_1$ ), Au dimer ( $\text{Au}_2$ ), Au trimer ( $\text{Au}_3$ ) and Au quatromer ( $\text{Au}_4$ ) on the lepidocrocite sheet is investigated. In each system every atom were free to relax and the vacuum between periodic images were at least  $10 \text{ \AA}$  to avoid any interaction. The same computational parameters were used as in the structural calculations for lepidocrocite sheets in Chapter 2. The Au pseudopotentials were again of the ultrasoft PBE type. We considered adsorption of all the  $\text{Au}_n$  forms for a  $(2 \times 2)$  unit cell with the exception of a brief investigation of  $\text{Au}_1$  adsorption on a  $(1 \times 1)$  cell. We also considered  $\text{Au}_1$  and  $\text{Au}_2$  adsorption at an O vacancy site. In all cases, we examined adsorption on a single side of the lepidocrocite sheet, expect one symmetric model for the Au monomer.

We obtained the binding energies,  $E_b$ , by substracting the sum of the energies of the isolated nanosheet and the isolated adsorbant from the total energy of the system:

$$E_b = E_{tot} - (E_{sheet} + E_{ad}) \quad (3.1)$$

For Au monomers,  $E_{ad}$  is taken as the energy of an isolated Au atom calculated in a large supercell preventing Au–Au interaction. For  $\text{Au}_2$ ,  $\text{Au}_3$  and  $\text{Au}_4$ ,  $E_{ad}$  is the energy of the isolated clusters, hence  $E_b$  is the binding energy of the cluster as a whole.

### 3.1 Adsorption of Au Monomers

#### 3.1.1 Au<sub>1</sub> on the (1×1) Surface

We investigated the Au atom on a (1×1) cell starting from two initial configurations. In the first model, Au atom is placed above the non-bridging oxygen at the midpoint between the bridging oxygens and in the other the Au atom is situated at the midpoint between two bridging oxygens above the lower Ti atom. Both cases resulted in fairly similar structures. The Au atom arose from the surface and formed an Au monolayer weakly bonded to the lepidocrocite structure below. This distance is 3.58 Å for both of the cases. The lepidocrocite structure underneath the Au layer does not show any structural deformation. The initial Au-Au distance which is the same as the lattice parameters of the lepidocrocite sheet, i.e., 3.02 Å and 3.73 Å did not change upon relaxation. Top view of the relaxed structure of Au<sub>1</sub> situated above the non-bridging O is shown in Figure 3.1. The Au monolayer is physisorbed and the states in the gap originate solely from the Au network. The impurity states filling the band gap are largely dispersed due to strong Au–Au interaction. The total system is metallic.

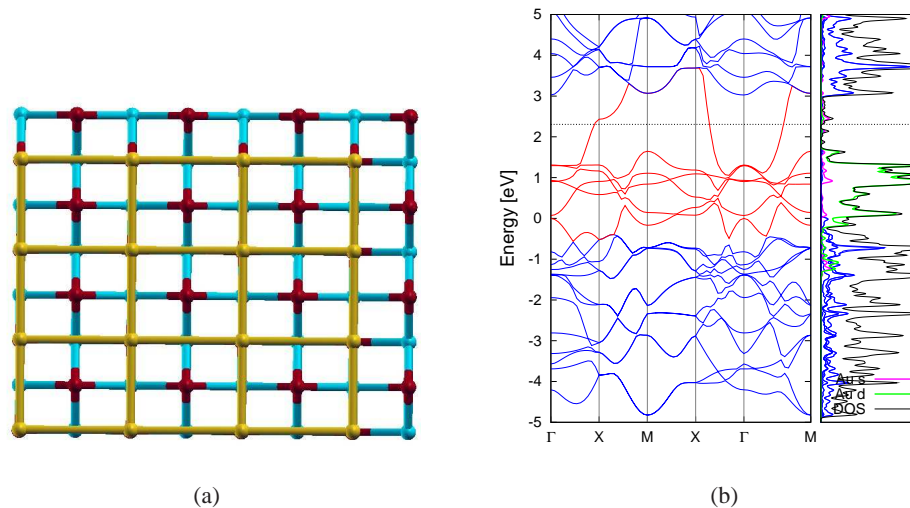


Figure 3.1: (1×1) adsorption of Au<sub>1</sub>: (a) Top view, (b) Band structure with DOS/PDOS.

### 3.1.2 Au<sub>1</sub> on the (2×2) Surface

In this section we considered Au adsorption on a (2×2) lepidocrocite surface. We investigated Au adsorption at 4 different sites on the lepidocrocite sheet. For each case the initial Au–Au distance is 6.04 Å in the (100) direction and 7.46 Å in the (010) direction. The sites considered are the top of the bridging O<sub>2c</sub> atom (site O1), top of the upper Ti<sub>6c</sub> atom (site Ti1), top of the non-bridging O<sub>4c</sub> atom (site O2) and top of the lower Ti<sub>6c</sub> atom (site Ti2). To be more clear, O1 is the surface oxygen and Ti1, O2 and Ti2 are of increasing order in terms of their depth from surface. Calculated binding energies and relevant bond lengths of the relaxed structures are summarized in Table 3.1.

Among the cases considered, Au on O1 gives the second highest binding energy. Au atom is positioned at 2.19 Å above O1 and it caused a slight raise of the O1 atom causing the O1-Ti1-O1 angle reduce by 4° to 108° and the Ti1-O1 distances became 1.88 Å. The effect of adsorption on the rest of the lattice is negligibly small. The relaxed structures and band structures are presented in Figure 3.2. As seen from the band structure, the defect states originating mainly from Au atoms fall in the band gap. These bands are almost flat as the Au-Au interaction on the (2x2) surface is negligibly small. The impurity state right below the conduction band consisting mostly of half-filled Au *s* orbitals, leads the system to a metallic state. The *p* orbitals of the O1 atom and the *d* orbitals of the Ti1 atoms interacting with Au has a slight contribution to this state as well. The remaining five defect states, are mainly due to Au *d* orbitals with some contribution from O1 atom and a weak Ti1 contribution. The uppermost one among these five locates 1.65 eV below the Fermi level.

Adsorption on Ti1 (Fig. 3.3) has the weakest binding energy and the distortion of the surface is almost absent due to weak Au interaction. Similar to the O1 case, an impurity state of mostly Au *s* orbitals is onto the Fermi level just below the conduction band. This system is metallic also. The remaining impurity bands start from 1.20 eV below the Fermi level. Ti1 *d* orbitals has a contribution to the uppermost defect band originating mainly from Au *s* attributed to the Au-Ti1 interaction. The lower Au *d* impurity bands have contributions from the two O1 atoms that the Au monomer is bonded to, and some from the *d* orbitals of the Ti1 and Au atoms.

The preferred adsorption site for Au monomer corresponding to the highest binding energy is the O2 site at which the Au atom is bonded to four bridging oxygens and two Ti1 atoms (Fig. 3.4). The O1 atoms are repelled due to the presence of the Au atom in their mid point and the O1-O1 distance at the adsorption site obtained a value of 3.88 Å while it became 3.60 Å at the empty parts. The Fermi level is pinned again by the half-filled Au *s* impurity state, making the system metallic. The lower defect states are at a distance of 1.55 eV to the Fermi level. The main contribution to the single Au *s* defect state comes from the Ti1 atoms that are not bonded to the Au atom. The O1 atoms and Ti1 atom interacting with Au has some weak contributions also. The upper one of the Au *d* bands has contributions from the Au-interacting Ti1 atoms with some contribution from the *d* orbitals of noninteracting Ti1. The main contribution from the surface atoms to the other defect bands comes from the O2 atom which is underneath the Au atom.

For this site we also investigated a symmetric model by attaching another Au atom at the same site on the other side of the sheet (Fig. 3.4.). No significant changes in the lattice structure occur compared to the asymmetrical case. The bond distances for Au<sub>1</sub> adsorption on O2 on a single face are valid for the Au adsorbed on both sides as well. The binding energy per Au atom is slightly higher by 0.01 eV in the symmetric case. In the symmetric model, there are twice as more impurity bands but those coming from the upper and lower Au atoms almost overlap and the band structure is very similar to the non-symmetric case. Distinct bands are visible in the states crossing the Fermi level.

Another weak interaction is observed when the Au atom is placed above the Ti2 atom (Fig 3.4). Despite the low binding energy, the lattice distortion is significant in the bridging oxygens. The repulsed O1 making Au bonds assumed an inter distance of 3.97 Å and 3.49 Å in the clean directions. Contrary to the other (2×2) Au<sub>1</sub> adsorption models, a defect site inside the band gap that pins the Fermi level is absent in this system. Most of the defect sites fall in the conduction or the valence band, leaving 2 impurity bands inside the gap right above the valence band. The upper defect band is 2.58 eV below the conduction band minimum. The Fermi level is situated inside the conduction band, very close to the lower edge, indicating that the system is metallic. In this case, both of the impurity bands are mainly due to the *d* orbitals of the Au atom.

The  $s$  orbital states appear mostly inside the conduction band. The upper defect band is has some contribution from the bridging oxygens bonded to the Au atom. The lower one is due to the  $s$  orbital as well as the  $d$  orbitals of the Au atom and the O2 atoms close to the Au impurity has some contribution.

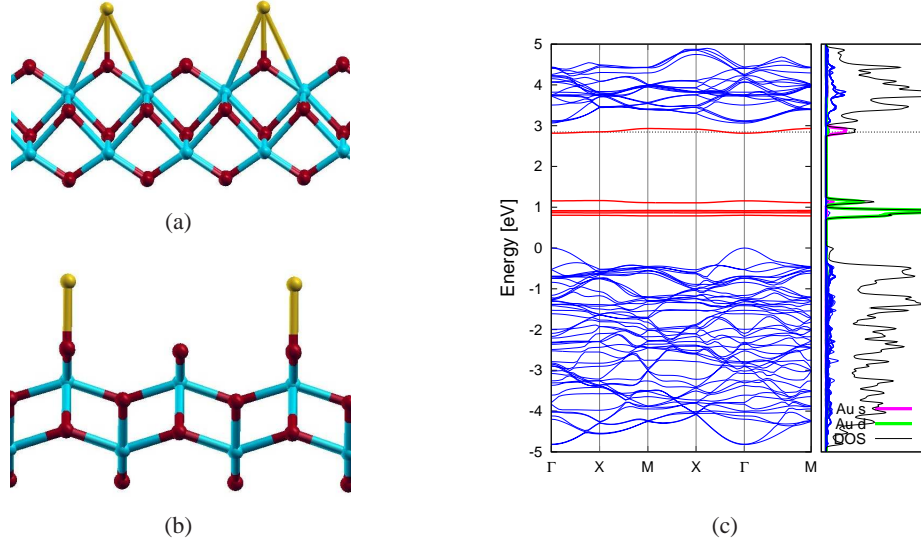


Figure 3.2:  $(2 \times 2)$  adsorption of  $\text{Au}_1$  on O1: (a) Side view along  $(100)$ ; (b) Side view along  $(010)$  and (c) Band structure with DOS/PDOS

Table 3.1: Calculated binding energies ( $E_b$ ), Fermi levels ( $E_f$ ) relative to the valence-band top, and the distances that the Au atom makes with the surface O and Ti atoms for Au monomer adsorption models on a  $(2 \times 2)$  surface.

Site	$E_b$ [eV]	$E_f$ [eV]	$d_{\text{Au-O1}}$ [ $\text{\AA}$ ]	$d_{\text{Au-Ti1}}$ [ $\text{\AA}$ ]
O1	0.27	2.84	2.19	3.63
Ti1	0.14	2.71	2.78	3.37
O2	0.31	2.29	2.80	2.98
$\text{O2}_{\text{sym}}$	0.32	2.26	2.80	2.98
Ti2	0.18	3.06	1.08	3.01

### 3.2 Adsorption of Au Dimers

The initial configuration possibilities for an Au dimer is much higher than the single atom case as the dimer can be positioned horizontally, vertically or diagonally. We started by considering five different initial configurations and ended up with four distinct structures as two models assumed the same final structure. The calculated

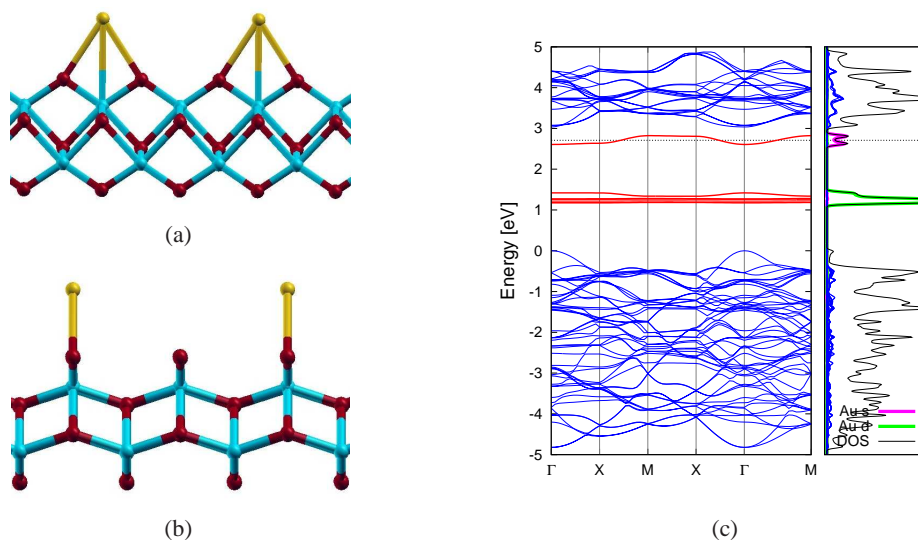


Figure 3.3: ( $2\times 2$ ) adsorption of  $\text{Au}_1$  on Ti1: (a) Side view along (100); (b) Side view along (010) and (c) Band structure with DOS/PDOS.

physical quantities for adsorption of  $\text{Au}_2$  are presented in Table 3.2.

Both the dimer which is oriented vertically above Ti2 at the midpoint between two bridging oxygens and the dimer which is oriented horizontally along (010) situated at the same place with its center of mass above Ti2, relaxed to the same structure (Fig. 3.5). This final structure is an inclined Au dimer making an angle of  $68^\circ$  with the surface plane. The Au atom closer to the surface ( $\text{Au}_1$ ) is bonded to a single bridging oxygen and to two nearby Ti1 atoms. The Au-Au distance of the dimer which is  $2.48 \text{ \AA}$  for an isolated  $\text{Au}_2$  did not change. The calculated binding energy for this configuration ( $0.77 \text{ eV}$ ) is the highest among other  $\text{Au}_2$  adsorption models and it is more than twice the highest binding energy obtained for Au monomers.

An initial configuration of the dimer oriented horizontally but placed diagonally between bridging oxygens such that its center of mass is situated above O2 obtained a final structure that is similar to the  $\text{Au}_2$ -Ti2 cases (Fig 3.6). Making an angle of  $53^\circ$  with the surface, it is more inclined and it preserves its diagonal orientation by Au2 pointing to the bridging O across the one Au1 is bonded to. Due to this diagonality, Au1 is closer to one of the two Ti1, hence makes a single Ti1 bond. The binding energy is smaller by about  $0.1 \text{ eV}$  compared to the  $\text{Au}_2$ -Ti2 model.

Two other cases investigated for  $\text{Au}_2$  adsorption are vertically and horizontally placed

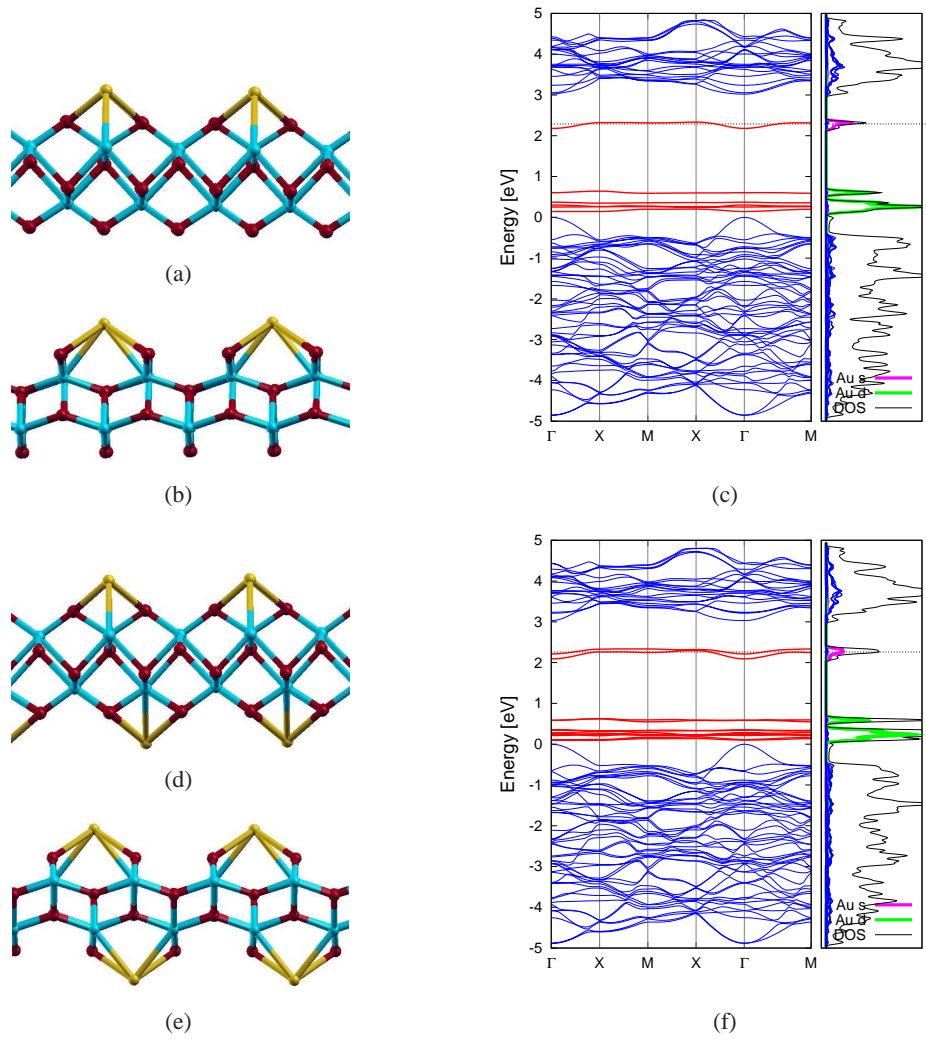


Figure 3.4:  $(2 \times 2)$  adsorption of  $\text{Au}_1$  on  $\text{O}_2$  on a single side [(a),(b) and (c)] and on both sides [(c),(d) and (e)]: (a),(d) Side view along (100); (b),(e) Side view along (010) and (c),(f) Band structure with DOS/PDOS.

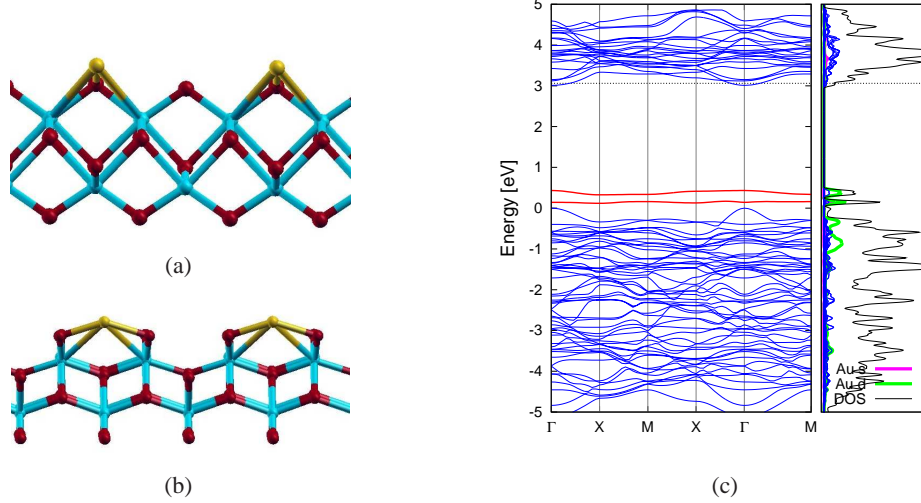


Figure 3.5:  $(2 \times 2)$  adsorption of  $\text{Au}_1$  on  $\text{O}_2$ : (a) Side view along  $(100)$ , (b) Side view along  $(010)$  and (c) Band structure with DOS/PDOS.

dimers above  $\text{O}_2$  (Fig. 3.7 and Fig 3.8). In both cases, without changing the initial orientation in any direction, the dimer just moved away from the surface resulting in weak binding energies. The vertical distance of the horizontal dimer from the  $\text{O}_1$  atoms is  $3.29 \text{ \AA}$ . Although this dimer has the lowest binding energy, it has the widest band gap.

Table 3.2: Calculated binding energies ( $E_b$ ), Fermi levels ( $E_f$ ) relative to the valence-band top, band gap values ( $E_g$ ) and the distances of adsorbed Au dimers

System	$E_b$ [eV]	$E_f$ [eV]	$E_g$ [eV]	$H_{surf}$ [ $\text{\AA}$ ]
$\text{O}_1$	0.77	2.79	0.63	1.90-4.12
$\text{O}_{1diag}$	0.65	2.67	0.94	1.44-2.81
$\text{O}_{2vert}$	0.25	2.53	0.91	2.05-4.55
$\text{O}_{2horz}$	0.24	2.48	1.19	3.29-3.29

### 3.3 $\text{Au}_1$ and $\text{Au}_2$ Adsorption at O Vacancy

Adsorption of an Au monomer and a vertically oriented Au dimer at an O defect site is investigated in this section. In calculating the binding energies from Eq. (3.1),  $E_{sheet}$  is replaced by  $E_{vac}$  corresponding to the total energy of the sheet with an oxygen vacancy whose properties were studied in Chapter 2. The calculated values for the

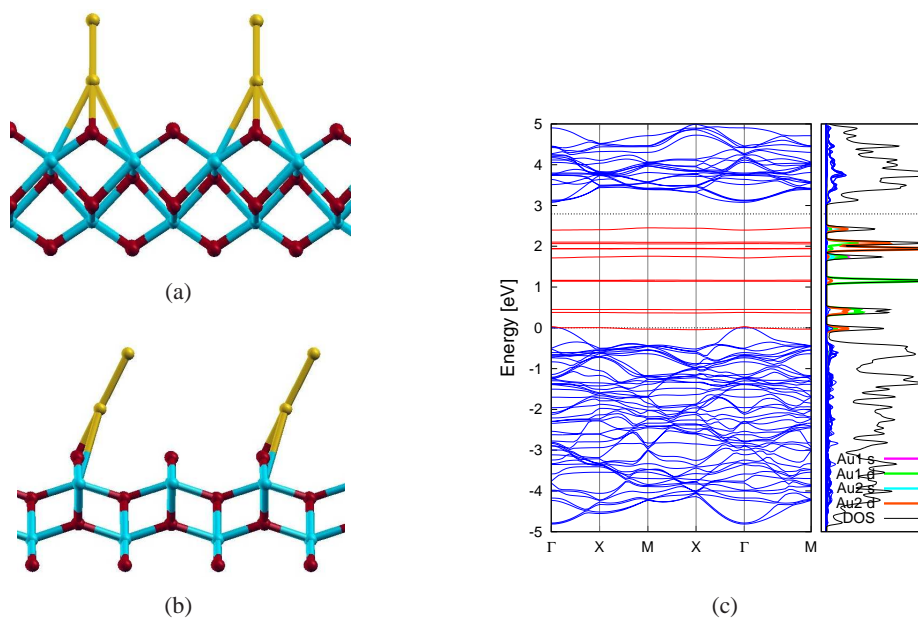


Figure 3.6:  $(2 \times 2)$  adsorption of  $\text{Au}_2$  on O1: (a) Side view along (100); (b) Side view along (010) and (c) Band structure with DOS/PDOS.

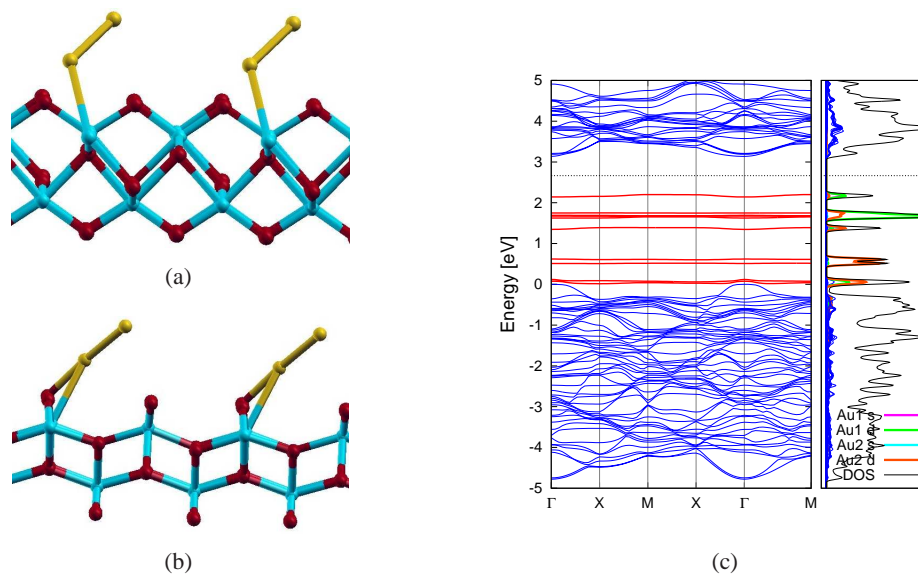


Figure 3.7:  $(2 \times 2)$  adsorption of  $\text{Au}_2$  diagonally positioned on O1: (a) Side view along (100); (b) Side view along (010) and (c) Band structure with DOS/PDOS.

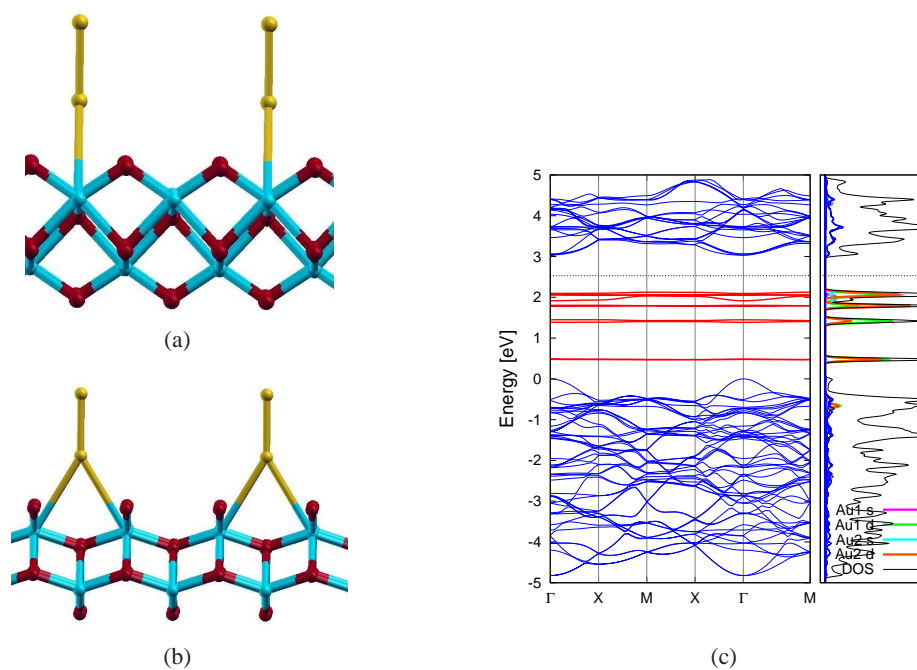


Figure 3.8:  $(2 \times 2)$  adsorption of vertically oriented  $\text{Au}_2$  on  $\text{O}_2$ : (a) Side view along  $(100)$ ; (b) Side view along  $(010)$  and (c) Band structure with DOS/PDOS.

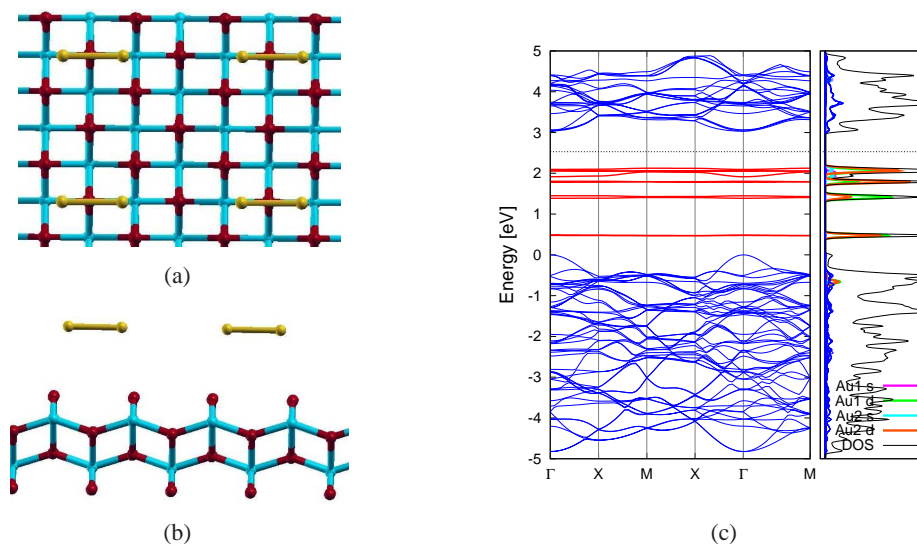


Figure 3.9:  $(2 \times 2)$  adsorption of horizontal  $\text{Au}_2$  on  $\text{O}_2$ : (a) Top view; (b) Side view along  $(010)$  and (c) Band structure with DOS/PDOS.

binding energies are several times larger than those for the clean surface adsorption cases. Thus, adsorption of Au atoms at O vacancies is highly favored compared to the defect free surface.

Relaxed structure Au<sub>1</sub> adsorption at the O vacancy is shown in Figure 3.9. The calculated binding energy is 3.54 eV. The presence of Au do not disturb the structure further than induced by the vacancy and the Ti1-Ti1 distance remains 3.19 Å around vacancy and 2.85 Å under the bridging O. The Au-Ti1 distance is 2.58 Å and the Ti1-Au-Ti1 angle is 76°. The band gap contains a single defect state. Most of the other Au impurity states are situated in the valence band. The Fermi level is located just at the conduction band edge manifesting metallicity. The single defect band is situated 2.33 eV below the conduction band minimum. It originates mainly from Au *s* orbital with some contribution from the *d* orbitals.

The binding energy of the Au dimer adsorped at the O defect is 2.92 eV which is 0.6 eV smaller than the monomer case. Au<sub>2</sub> had a slight constructive effect on the lattice such that the defect neighboring Ti1 become closer with a distance of 3.08 Å and underneath O1, it increased to 2.96 Å accordingly . Upon adsorption, the Au-Au distance increased from 2.48 Å to 2.54 Å. The Au1-Ti1 distance is also equal to 2.54 Å with a corresponding Ti1-Au1-Ti1 angle of 75°. As the band structure displays, the system is a semiconductor with a band gap of 0.56 eV, smaller than those of the Au<sub>2</sub> adsorption on a clean surface. There are 7 impurity bands inside the band gap some of which are highly overlapping. The upmost single impurity band comes mostly from the *s* orbital of the upper Au atom. The *p* and the *d* orbitals of the same atom and the *d* orbitals of neighboring Ti1 atoms contribute this state also. The following band, consisting of two overlapping bands is mainly due to the *d* orbitals of Au2. The band strip right below actually is formed from 3 bands. These bands consist again of the Au2 *d* orbitals with some contribution from *d* and *p* orbitals of the lower Au atom, and Ti1 *d* orbitals. The last single impurity band originates from the *s* and *d* orbitals of the Au1, along with a weak contribution from Au2 *s* orbital.

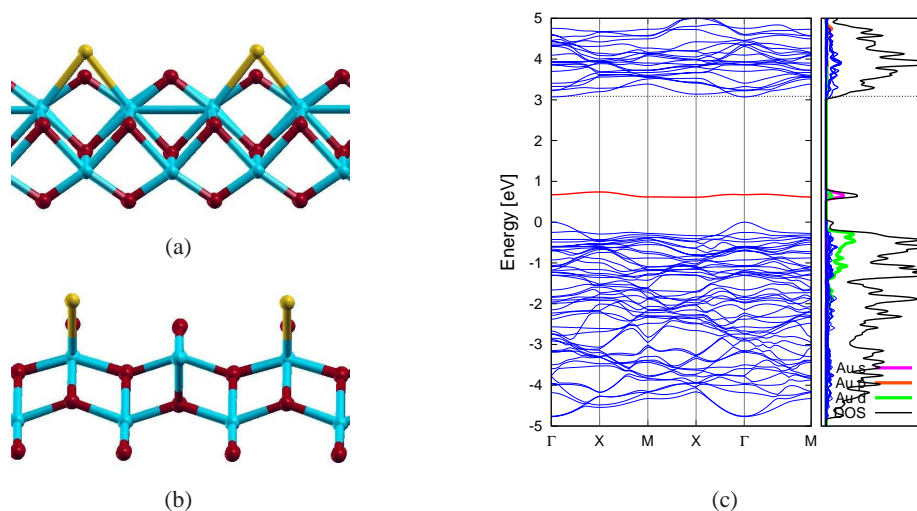


Figure 3.10:  $(2 \times 2)$  adsorption of  $\text{Au}_1$  at O vacancy: (a) Side view along  $(100)$ ; (b) Side view along  $(010)$  and (c) Band structure with DOS/PDOS.

### 3.4 Adsorption of Au Trimers and Au Quatromers

A triangularly shaped  $\text{Au}_3$  is initially put above the bridging O atom in an upside-down manner so that the lower Au atom is attached to O1. They were oriented in a diagonal fashion. During relaxation, the  $\text{Au}_3$  clusters rotated, became co-planer and the Au atoms made bonds with each other. The relaxed structure is an Au chain elongating in the  $(100)$  direction as shown in Figure 3.6. Due to strong Au-Au interaction, Au bands are greatly highly degenerate and the system is metallic as seen from the band structure (Fig.3.6).

Another  $\text{Au}_3$  cluster, having a linear shape is initially placed vertically above O2 with the Au atom closest to the surface making two O bonds with the bridging oxygens. The relaxed system and the band structure is shown in Figure 3.13. Upon relaxation the cluster obtain a zig-zag like shape but did not interacted with neighbouring clusters as depicted from flat bands in the band structure. Like in the case with Au dimers, the lowermost Au atom stayed bonded to a single bridging O atom. The binding energy is weak, calculated to be 0.40 eV. The relaxed system and the band structure is shown in Figure 3.7. The system is metallic.

A single case for the  $\text{Au}_4$  cluster have been considered. The most stable geometry of  $\text{Au}_4$  clusters is predicted to be a planar rhombus by previous theoretical studies

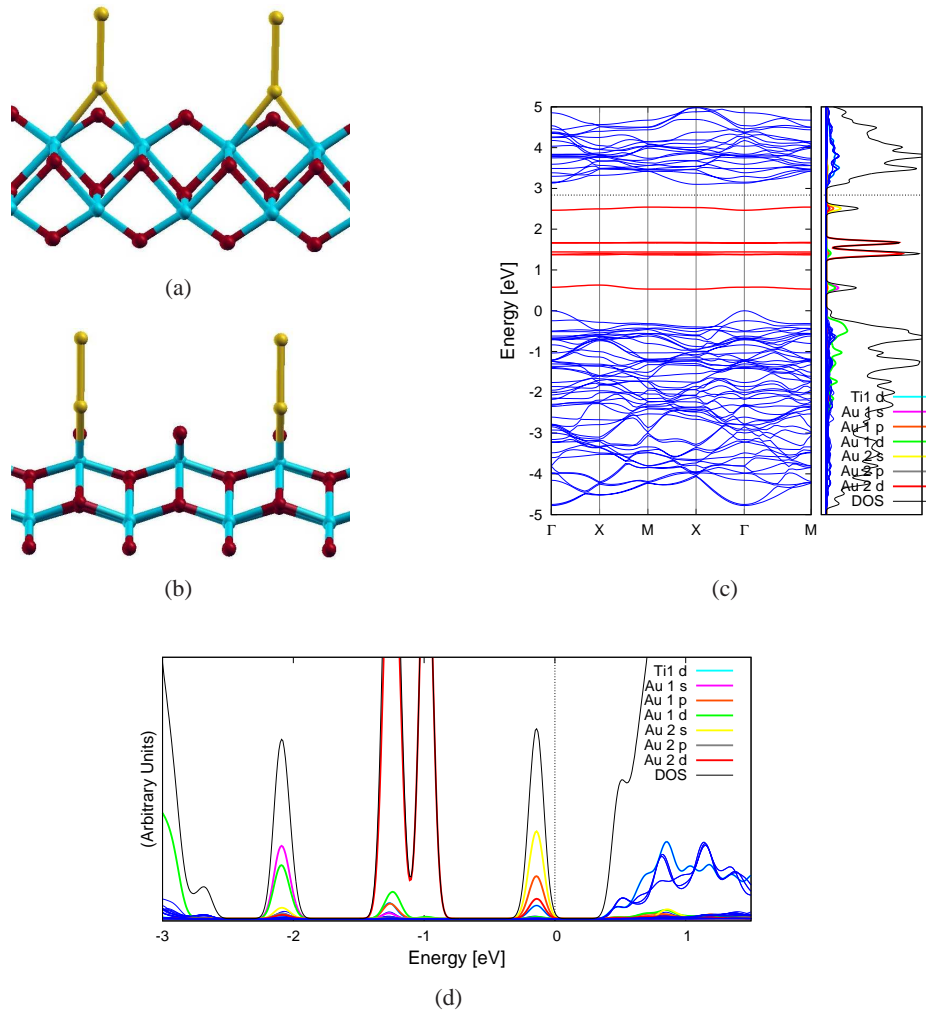


Figure 3.11:  $(2 \times 2)$  adsorption of  $\text{Au}_2$  at O vacancy: (a) Side view along (100); (b) Side view along (010); (c) Band structure with DOS/PDOS and (d) PDOS detail around the band gap.

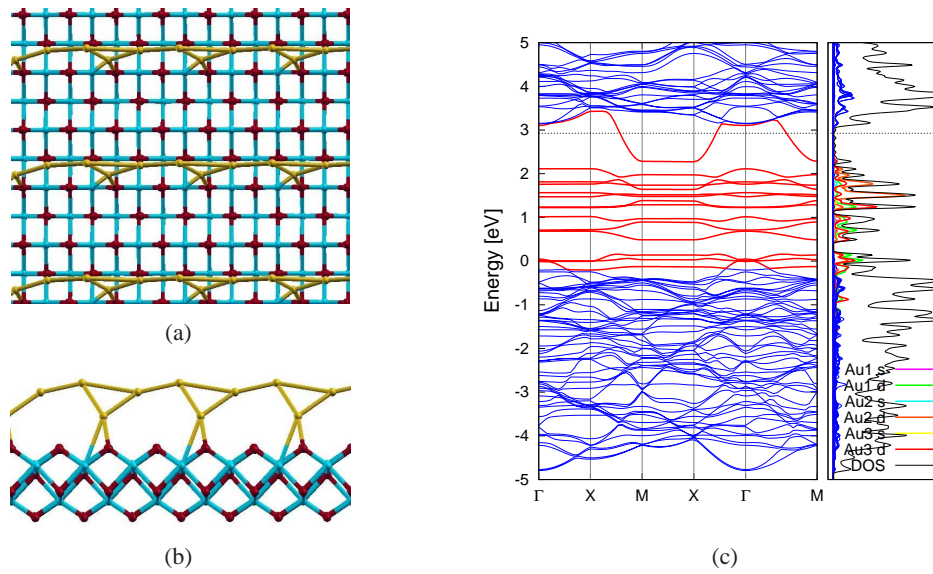


Figure 3.12: Relaxed structures of triangular  $\text{Au}_3$  forming a chain: (a) Top view, (b) Side view along (100) and (c) Band structure with DOS/PDOS.

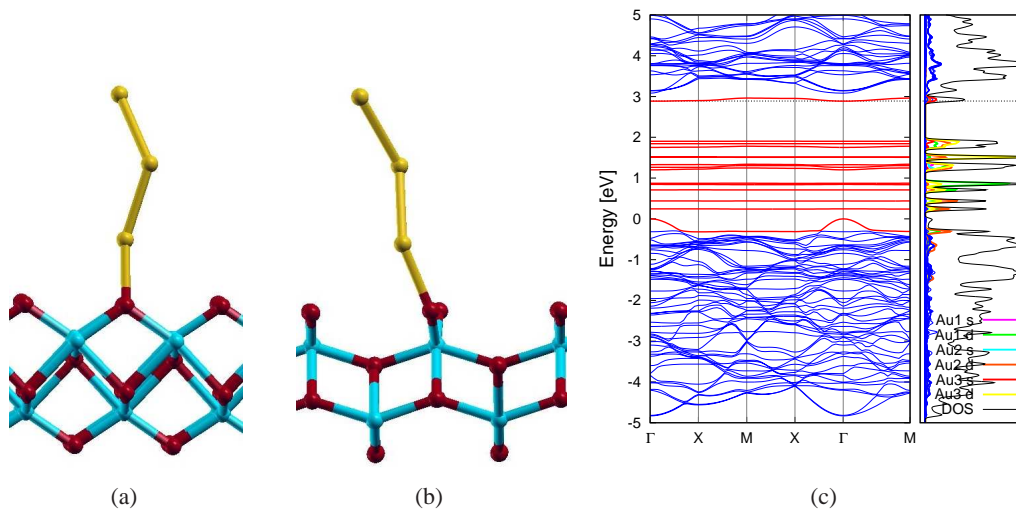


Figure 3.13:  $(2 \times 2)$  adsorption of  $\text{Au}_3$  on O1: (a) Side view along (100), (b) Side view along (010) and (c) Band structure with DOS/PDOS.

[45]. However, as 2 or 3 dimensional clusters can easily interact on a (2x2) surface to form chains or layers as in the triangular Au<sub>3</sub> case, we considered a 1 dimensional linear Au<sub>4</sub> chain oriented vertically and initially positioned above site O2. Similar to the linear Au<sub>3</sub> model, the lowermost Au atom attach to O1 and the cluster assume a zig-zag linking. The binding energy is calculated to be 1.22 eV which is largest among all the adsorption cases on a clean surface.

As depicted from the band structure, the system is a semiconductor with a small band gap having a value of 0.46 eV. There are 20 impurity bands in the band gap region. As seen from the PDOS detail (Fig. 3.14) the bands that are closer to the conduction band are mainly due to the upmost atoms in the chain, namely atoms Au<sub>4</sub> and Au<sub>3</sub>. The contribution of the O1 atom that Au<sub>1</sub> is bonded to is strongest in the bands closer to the valence band. The contribution of the interacting Ti1 atom is important in the bands lying around 1.5 eV in the band structure.

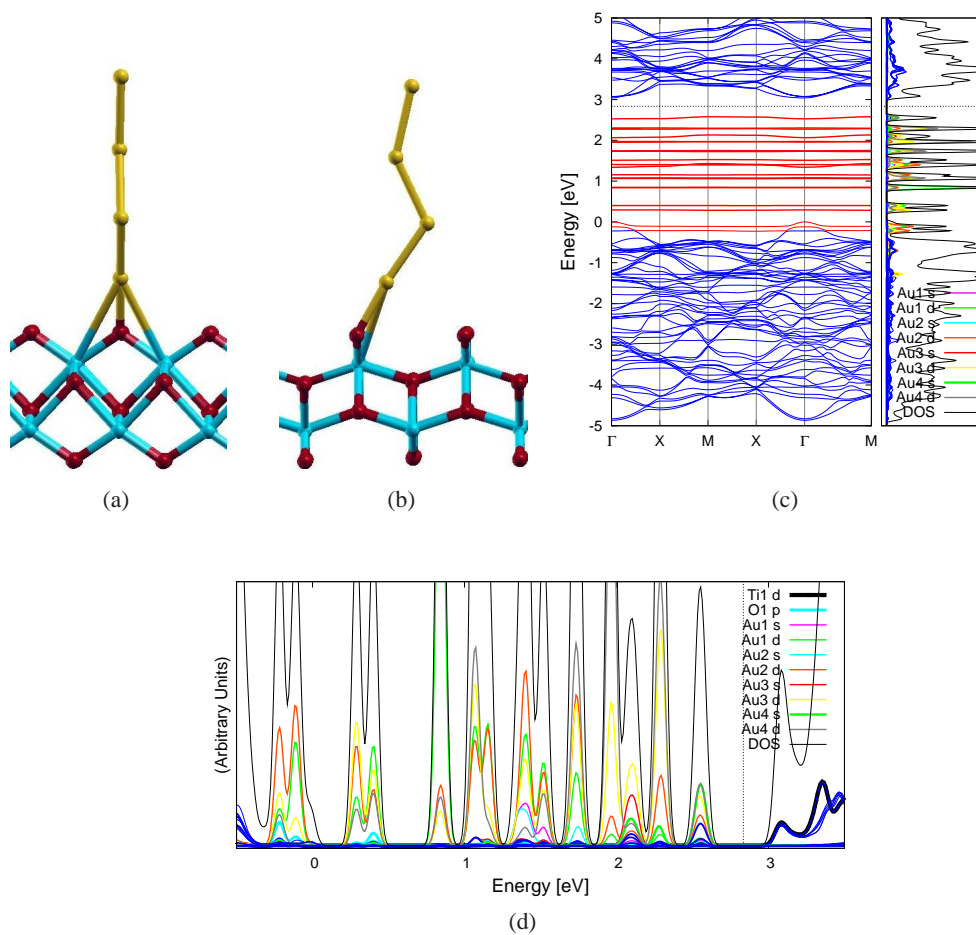


Figure 3.14: (2 $\times$ 2) adsorption of Au<sub>4</sub> on O1: (a) Side view along (100); (b) Side view along (010); (c) Band structure with DOS/PDOS and (d) PDOS detail around the band gap.

## CHAPTER 4

### CONCLUSION

In the bulk calculations for the anatase unit cell we showed that the variable-cell relaxation techniques can be used to obtain the lattice parameters of the tetragonal cell by using larger cut-off values than needed for regular fitting processes. Additionally, through DFT+U calculations, we found that the band gap of anatase which is underestimated by standard DFT calculations can be corrected to give values close to the experimental band gap. Furthermore, the DFT+U correction has little deformative effect on the lattice structure as observed through a variable-cell calculation. Upon optimisation of the anatase nanosheets delaminated from the (001) surface we observed that they tend to shrink to obtain smaller unit cells. We found that the lepidocrocite structure is the most stable nanosheet among those studied and it also has a significantly large band gap. The oxygen vacancy with a 25% concentration on the lepidocrocite sheet resulted in a visible deformation in the lattice structure and in a defect site just below the conduction band in the band structure.

From the investigation of nanotubes we conclude that the lepidocrocite nanotubes below a certain radius are not stable. The smallest stable nanotube we obtained has a diameter of 1.5 nm. The stability of the nanotubes increases with increasing diameter such that the nanotube with a diameter of 2.6 nm is twice more stable than that with a diameter of 1.5 nm. The band gap of the nanotubes widens by increasing diameter, however for the cases we studied, they did not exceed the gap of the flat lepidocrocite sheet. They have indirect band gaps as the anatase nanosheets and the dispersion of the bands were not large.

In our adsorptional studies, we found that Au monomers adsorbed on a (1x1) surface

tend to form an Au layer that is several angstroms above the surface. For the (2x2) Au monomer adsorption cases, the Au monomers bind to the surface with small binding energies and metallizes the surface. The favored adsorption site of the monomer is above the surface Ti atom. There is not a one-to-one correspondence with the Au monomers binding energy and its distance to the surface atoms or the distortions it induced on the surface structure. On the other hand, Au dimers adsorbed with 0.25 ML concentration has higher binding energies and dimer adsorbed lepidocrocite sheets are small band gap semiconductors which is a desired property in photocatalytic systems. The band gap is about one fifth of the clean lepidocrocite structure. An inclined Au dimer that is bonded to the surface bridging oxygen is the favored configuration. Au absorption at O vacancy is the most preferred case with large binding energies. This result is in accordance with previous results about Au adsorption on TiO<sub>2</sub> [57]. Adsorbed Au clusters having 3 atoms are metallic as Au monomers. Triangular Au trimer clusters formed a two dimensional chain on the surface with largely dispersed and degenerate defect bands filling the band gap. Adsorbed linear Au trimer results in a metallic system too and as Au dimers it prefers attaching to the bridging oxygen atom. Au quatramer adsorption is similar to the Au dimer cases such that the system becomes a narrow band gap semiconductor. The binding energy of Au<sub>4</sub> is the largest among absorptional studies on the clean surface. Thus, we can infer that small Au clusters having an even number of Au deposited on the surface makes the system a semiconductor with a narrowed band gap which has the potential to be photocatalytically active under visible light. All the Au clusters with more than 1 atom, bonded to the bridging O on the defect free surface. However, on the overall an oxygen vacancy is preferred. The best configuration in term of photocatalysis seems to be the Au dimer adsorbed at the Au vacancy as it both has a large binding energy (2.9 eV) and it is narrow band gap semiconductor.

## REFERENCES

- [1] B. O'Regan and M. Gratzel, *Nature* **353**, 737 (1991).
- [2] T. Bak, J. Nowotny, M. Rekas and C. C. Sorrell, *Int. J. Hydrogen Energy* **27**, 991 (2002).
- [3] Y. Paz, Z. Luo, L. Rabenberg and A. Heller, *J. Mat. Research* **10**, 2842 (1995).
- [4] L. D. Birkefeld, A. M. Azad and S. A. Akbar, *J. Am. Ceramic Soc.* **75**, 2964 (1992).
- [5] A. Mills, R. H. Davies and D. Worsley, *Chem. Soc. Rev.* **22**, 417 (1993).
- [6] F. Croce, G. B. Appetecchi, L. Persi and B. Scrosati, *Nature* **394** 456 (1998).
- [7] A. L. Linsebigler, Guangquan Lu and J. T. Yates, *Chem. Rev.* **95**, 735 (1995).
- [8] M. R. Hoffmann, S. T. Martin, W. Choi and D. W. Bahnemann, *Chem. Rev.* **95**, 69 (1995).
- [9] M. Born and J. R. Oppenheimer, *Ann. Phys.* **84**, 457 (1927).
- [10] C. Eckart, *Phys. Rev.* **46**, 383 (1935).
- [11] E. Fermi, *Proc. Cambridge Phil. Soc.* **23**, 542 (1927).
- [12] L. H. Thomas, *Rend. Accad. Naz. Lincei* **6**, 602 (1928).
- [13] P. Hohenberg and W. Kohn, *Phys. Rev.* **136**, B864 (1964).
- [14] W. Kohn and L. J. Sham, *Phys. Rev.* **140**, A1133 (1965).
- [15] J. P. Perdew and A. Zunger, *Phys. Rev. B* **23**, 5048 (1981).
- [16] J. P. Perdew and Y. Wang, *Phys. Rev. B* **45**, 13244 (1992).
- [17] A. D. Becke, *Phys. Rev. A* **38**, 3098 (1988).
- [18] C. Lee, W. Yang and R. G. Parr, *Phys. Rev. B* **37**, 785 (1988).
- [19] J. P. Perdew, K. Burke and M. Ernzerhof *Phys. Rev. Lett.* **77**, 3865 (1996).
- [20] S. Baroni, A. Dal Corso, S. de Gironcoli, P. Giannozzi, C. Cavazzoni, G. Balabio, S. Scandolo, G. Chiarotti, P. Focher, A. Pasquarello, K. Laasonen, A. Trave, R. Car, N. Marzari and A. Kokalj. <http://www.pwscf.org/>.
- [21] C. Kittel, *Introduction to Solid State Physics* (Wiley, 1996).
- [22] R. M. Martin, *Electronic Structure* (Cambridge University Press, 2004).

- [23] R. G. Parr and W. Yang, *Density-Functional Theory of Atoms and Molecules* (Oxford University Press, 1989).
- [24] H. J. Monkhorst and J. D. Pack, *Phys. Rev. B* **13**, 5188 (1976).
- [25] D. R. Hamann, M. Schlüter and C. Chiang, *Phys. Rev. Lett.* **43**, 1494 (1979).
- [26] D. Vanderbilt, *Phys. Rev. B* **41**, 7892 (1990).
- [27] C. G. Broyden, *Math. Comput.* **19**, 547 (1965).
- [28] E. R. Davidson, *J. Comp. Phys.* **17**, 87 (1975).
- [29] A. Fujishima and K. Honda, *Nature* **238**, 37 (1972).
- [30] U. Diebold, *Surf. Science Reports* **48**, 53 (2003).
- [31] T. Ohno, K. Sarukawa, K. Tokieda and M. Matsumura, *J. Catalysis* **203**, 81 (2001).
- [32] A. Vittadini, A. Selloni, F.P. Rotzinger and M. Graetzel, *Phys. Rev. Lett.* **81**, 2954 (1998).
- [33] T. Sasaki, Y. Ebina, Y. Kitami, M. Watanabe, *J. Phys. Chem. B* **105**, 6116 (2001).
- [34] P. Weng, H. Itoh, W. Tang and Q. Feng, *Langmuir* **23**, 11782 (2007).
- [35] T. Orzali, M. Casarin, G. Granozzi, M. Sambì and A. Vittadini, *Phys. Rev. Lett.* **97**, 156101 (2006).
- [36] Y. Zhang, L. Giordano, G. Pacchioni, A. Vittadini, F. Sedona, P. Finetti and G. Granozzi, *Surf. Sci.* **601**, 3488 (2007).
- [37] G. Mogilevsky, Q. Chen, H. Kulkarni, A. Kleinhammes, W.M. Mullins and Y. Wu, *J. Phys. Chem. C* **112**, 3239 (2008).
- [38] A. Vittadini and M. Casarin, *Theor. Chem. Account* **120**, 551 (2008).
- [39] G. K. Mor, K. Shankar, M. Paulose, O.K. Varghese and C.A. Grimes, *Nano Letters* **5**, 191 (2005).
- [40] G. K. Mor, O.K. Varghese, M. Paulose, K. Shankar and C.A. Grimes, *Solar Energy Mater. and Solar Cells* **90**, 2011 (2006).
- [41] T. Kasuga, M. Hiramatsu, A. Hoson, T. Sekino and K. Niihara, *Langmuir* **14**, 3160 (1998).
- [42] W. Wang, O. K. Varghese, M. Paulose, C. A. Grimes, Q. Wang and E. C. Dickey, *J. Mater. Res.* **19**, 417 (2004).
- [43] J. C. Hulteen and C. R. Martin, *J. Mat. Chem.* **7**, 1075 (1997).
- [44] J. K. Burdett, T. Hughbanks, G. J. Miller, J. W. Richardson, and J. V. Smith, *J. Am. Chem. Soc.* **109**, 3639 (1987).
- [45] M. Lazzeri, A. Vittadini and A. Selloni, *Phys. Rev. B* **63**, 155409 (2001).

- [46] M. Parrinello and A. Rahman, *Phys. Rev. Lett.* **45**, 1196 (1980).
- [47] R. M. Wentzcovitch, *Phys. Rev. B* **44**, 2358 (1991).
- [48] M. Cococcioni, *A LDA+U Study of Selected Iron Compounds*, (PhD. Thesis, SISSA) (2002).
- [49] B. Morgan and W. Watson, *Surf. Sci.* **601**, 5034 (2007).
- [50] D. Raczkowski, A. Canning and L. W. Wang, *Phys. Rev. B* **64**, R121101 (2001).
- [51] A. Kokalj, *Comp. Mater. Sci.* **28**, 155 (2003). <http://www.xcrysden.org/>.
- [52] N. Sakai, Y. Ebina and T. Sasaki, *J. Am. Chem. Soc.* **126**, 5851 (2004).
- [53] W. Choi, A. Termin and M. R. Hoffman, *J. Phys. Chem.* **98**, 13669 (1994).
- [54] M. Haruta and M. Date, *App. Catal. A-Gen.* **222**, 427 (2001).
- [55] M. Valden, X. Lai and D. W. Goodman, *Science* **281**, 1647 (1998).
- [56] E. W. McFarland and J. Tang, *Nature* **421**, 616 (2003).
- [57] A. Vittadini, M. Casarin and A. Selloni *Theor. Chem. Account* **117**, 663 (2007).
- [58] A. N. Enyashin and G. Seifert, *Phys. Stat. Sol. B* **242**, 1362 (2005).